ELECTRONIC AND OPTOELECTRONIC DEVICES USING EPITAXIAL VANADIUM DIOXIDE

By

Jaeseong Lee

A dissertation submitted in partial fulfillment of

the requirements for the degree of

Doctor of Philosophy

(Electrical Engineering)

at the

UNIVIERSITY OF WISCONSIN-MADISON

2016

Date of final oral examination: 06/29/2016

The dissertation is approved by the following members of the Final Oral Committee:

Zhenqiang Ma, Professor, Electrical and Computer Engineering

Chang-Beom Eom, Professor, Materials Science and Engineering

Zongfu Yu, Assistant Professor, Electrical and Computer Engineering

Hongrui Jiang, Professor, Electrical and Computer Engineering

Xinyu Zhang, Assistant Professor, Electrical and Computer Engineering

Abstract

Phase transitions in correlated oxide materials can be manipulated to yield emergent functional properties, promising new paradigms for electronics and optoelectronics. Vanadium dioxide (VO_2) is one of the most attractive correlated oxide materials that exhibit a sharp insulator-to-metal phase transition (IMT) along with structural phase transition (SPT) from the monoclinic insulating phase to the tetragonal metallic phase at 341 K. It is critical to fully exploit the transition properties to develop high performance application devices. Up to date, however, growing high quality VO_2 thin films has been a challenge. Thus, polycrystalline VO_2 films with degraded phase transition properties have been used for applications, which limit the development of high performance application devices.

In this thesis, electronic and optoelectronic devices are demonstrated using highly epitaxial VO_2 grown on on TiO_2 (001) substrate with a SnO_2 template layer. The electrical and optical properties of the newly developed epitaxial VO_2 were analyzed, which were as good as properties of single crystalline bulk VO_2.

Thermally triggered RF switches show that fast IMT at a low temperature allowed VO_2 RF switches to exhibit sharp resistivity changes with the S_{21} change greater than 15 dB at 333 K and 339 K for IMT and MIT, respectively. The sharp phase transition results in the full width at half-maximum (FWHM) of S_{21} change less than 3 K, and the cut-off frequency (F_{co}) was 18.9 THz.

Electrically triggered RF switches show the turn-on voltage of 13.1 V and resistivity change of 4 orders of magnitude. The switches exhibit the 3 dB operation frequency over 24 GHz by both electrical and thermal excitations, which confirms that the phase transition can be fully triggered

only by applying voltage bias. The study on electrical switching dynamics revealed 840 ns for IMT switching time.

For the optoelectronic application, Si-VO_2 integrated optical switches were demonstrated. Since the optical properties of VO_2 were not ideal to be used alone as an optical waveguide core, Si waveguide was integrated by the nanomembrane transfer printing method. The optical switch is ON-state in metallic phase VO_2 and OFF-state in insulator phase. When 15 V DC bias was applied, the extinction ratio of 13.83 dB and insertion loss of 3.41 dB for the wavelength of 1550 nm were observed. The switching time measured with square wave voltage showed turn on and off time of ~ 150 ns and ~ 250 ns, respectively.

Acknowledgements

First and foremost, this work would not have been possible without the faithful support from my wife Woojung and family. They have encouraged me and trusted in me to finish this journey over the last five years. No words are sufficient to thank them here.

I would like to express my sincere gratitude to my advisor, Professor Zhenqiang (Jack) Ma for his guidance, patience and support. He has been constantly diligent and motivating. It was my honor to study and work under his supervision. I would like to thank Professor Chang-Beom Eom for his advice and sharp insights. His critical thinking and pursuit of excellence have enlightened my approach to research. I would like to thank Office of Naval Research (N00014-13-1-0183) and Kwanjeong Educational Foundation for providing the grant that supports the research.

I would also like to thank my research group members, university staff, and all my colleagues. They have provided valuable inputs to my work. Countless discussions have led me to the right direction through the research. Days and nights we spent together in the cleanroom and the labs are unforgettable memories.

Lastly, I would like to thank my friends for their encouragement and prayers. Warm friendship helped me to fight during my hard times. They have supported me and my family with love and kindness. Their companionship has made my Ph.D. life much more joyful.

Table of Contents

Abstract i

Acknowledgements iii

Table of Contents iv

List of Figures vi

List of Tables x

1. Introduction 1

 1.1. Correlated oxide materials 1

 1.2. Phase transition mechanism of VO_2 2

 1.3. Growth of highly epitaxial VO_2 thin films 4

 1.4. Thesis organization 6

2. Properties of VO_2 8

 2.1. Phase transition property changes by growth conditions 8

 2.2. Electrical properties of epitaxial VO_2 10

 2.3. Optical properties of epitaxial VO_2 11

3. Epitaxial VO_2-based RF Switches with Thermal Excitation 14

 3.1. Conventional RF switches 14

 3.2. Previous RF switches based on phase change materials 16

 3.3. Device design and fabrication 18

 3.4. Device characterization 19

 3.5. Summary 25

4. Epitaxial VO_2 based RF Switches with Electrical Excitation 27

4.1. Previous electrically triggered RF switches based on VO_2 27

4.2. Device design and fabrication 28

4.3. DC characterization 30

4.4. RF characterization 32

4.5. IMT switching speed characterization 36

4.6. Summary 38

5. Silicon nanomembrane transferred optical switches on epitaxial VO_2 40

5.1. Previous optical application devices based on VO_2 40

5.2. Optical switching device design 41

5.3. Device fabrication 44

5.4. Device characterization 46

5.5. Summary 50

6. Conclusion 52

Appendix 55

A. Optical constants of VO_2 55

A.1. Optical constants vs. temperature 55

A.2. Optical constants vs. wavelength 58

B. Fabrication process for Si- VO_2 integrated optical switches 63

B.1. Dry etching of VO_2 63

B.2. Si nanomembrane (NM) transfer printing 65

B.3. Optical waveguide patterning on Si 69

B.4. Metal electrode deposition 70

References 72

List of Figures

Figure 1.1 Schematic lattice structure and band diagram of VO_2 for insulating and metallic phase. (a) Cross sectional view of crystal lattice structure change of VO_2. (b) Band diagram change of 3d bands near the Fermi level for VO_2.. 3

Figure 1.2 XRD φ scan of the off-axis (112) reflections of (top) TiO_2, (center) SnO_2, and (bottom) VO_2, clearly indicating the epitaxial growth of VO_2 6

Figure 2.1 Issues for VO_2 thin films associated with different growth conditions. (a) Hysteresis loop gap change by growth method[31]. (b) Cracks due to the large tensile strain in the films[32]. (c) Resistance change ratio difference depending on substrate[33]. (d) Resistivity change ratio difference depending on growth methods[34]. 9

Figure 2.2 Electrical resistivity for VO2 films as a function of temperature.............................. 10

Figure 2.3 Optical constants change during IMT in VO_2 film. (a), (b) Refractive index *n* as functions of T and wavelength λ for 300-nm-thick VO_2 films on TiO_2 (a) and SnO_2/TiO_2 (b). (c), (d) Extinction coefficient *k* as functions of T and wavelength λ for 300-nm-thick VO_2 films on TiO_2 (c) and SnO_2/TiO_2 (d).. 12

Figure 2.4 Optical constants of VO_2 on SnO_2/TiO_2 for telecommunication wavelengths, 1310 and 1550 nm. (a) Refractive index, *n*. (b) Extinction coefficient, *k*. 13

Figure 3.1 Schematic cross section of conventional RF switches. (a) GaN based HFET solid-state RF switch[44]. (b) Al membrane based capacitive MEMS RF switch[40]................................ 15

Figure 3.2 Schematic cross section of RF switch based on phase change material, GeTe[54]. 17

Figure 3.3 (a) A schematic illustration of the fabrication process for epitaxial VO_2 based RF switches. (b) A microscopic image of the device and its dimensions. (c) A cross-sectional scanning electron microscope (SEM) image of the finished device... 19

Figure 3.4 The measured and simulated S_{11} and S_{21} characteristics of VO_2 RF switches (a) at the ON-state, and (b) at the OFF-state under a frequency range of 45 MHz to 40 GHz. (c) The measured and simulated group delay of the device. (d) The output RF power as a function of input RF power from -27 dBm to 3 dbm for various frequency points. 21

Figure 3.5 (a) An equivalent circuit model that was used to model VO_2 RF switches. (b) A simplified equivalent circuit model for the switch operation. At room temperature, the switch is at the ON-state and can be simplified to the RL series circuit. At above the IMT temperature, the switch is at the OFF-state and can be simplified to the RC parallel circuit. 22

Figure 3.6 (a) S_{21} curves for VO_2 RF switches under the heating and the cooling cycles by thermally triggered IMT. (b) Derivatives of S_{21} curve, d(S_{21})/dT to show the peaks and FWHM of IMT curves. 24

Figure 4.1 Phase transition characteristics of polycrystalline VO_2 on single crystalline sapphire substrate[29]. (a) The resistivity as a function of temperature by thermal phase transition. (b) The resistivity change as a function of voltage. 28

Figure 4.2 (a) A schematic illustration of the fabrication process for electrically triggered VO_2 RF switches. (b) A microscopic image. (c) A cross-sectional scanning electron microscope (SEM) image taken from the finished device. 29

Figure 4.3 DC characteristics of the VO_2 RF switches. (a) I-V characteristic of VO_2 switches in series with 1.5 to 6 kΩ resistors. (b) The VO_2 resistance as a function of series resistance extracted from slopes of I-V curves in Fig. 4.3 (a). 31

Figure 4.4 The measured and simulated S_{11} and S_{21} parameters of VO_2 RF switches in the frequency range from 45 MHz to 40 GHz (a) at the ON-state, and (b) at the OFF-state under a frequency range of 45 MHz to 40 GHz. 33

Figure 4.5 (a) An equivalent circuit model that was used to model VO_2 RF switches. (b) A simplified equivalent circuit model for the switch operation. The device is simplified to the RL series circuit at the ON-state and the RC parallel circuit at the OFF-state. 34

Figure 4.6 (a) A circuit schematic used to measure phase transition time. (b) Voltage response of the VO_2 RF switch with 1 kΩ series resistor under various frequencies from 10 kHz to 400 kHz. 36

Figure 5.1 The schematic illustration of the cross section for Si- VO_2 integrated optical switches. Design parameters for optimized geometry are shown such as Si waveguide thickness h_{Si}, Si waveguide width w, VO_2 layer thickness h_{VO2}, Su-8 layer thickness h_{Su8}, and spacing between metal comtact and waveguide *gap*. 42

Figure 5.2 The Si- VO_2 integrated optical switch design. (a), (b) Simulated electric field profile when the VO_2 is in insulator phase and metallic phase, respectively. (c) A diagram shows relation between the operation of the optical switch and the optical constants of the VO_2. 43

Figure 5.3 The fabrication process illustration. (a) Process illustration for preparing Si nanomembrane (NM). (b) Process illustration for fabricating an optical switch using Si NM and VO_2 on SnO_2/TiO_2. 45

Figure 5.4 Electrically triggered optical switch using epitaxial VO_2. (a), (b) Schematic drawings for the optical modulator consisting of single crystalline Si waveguide and epitaxial VO_2 film (a) without and (b) with applying an external voltage V_{dc}. (c), (d) Simulated TE mode light propagation through the Si waveguide for the light wavelength λ of 1.55 μm, when the VO_2 is in the (c) insulating and (d) metallic states. The VO_2 layer can be metallized by applying V_{dc}, which is higher than a threshold voltage for IMT 47

Figure 5.5 Electrically triggered light transmission in Si-VO_2 integrated optical switches. (a) Light transmission for the off (i.e., V_{dc} = 0 V) and on (i.e., V_{dc} = 15 V) state for a fixed wavelength λ of 1,550 nm. (b) The extinction ratio (ER) and the insertion loss (IL) of transmission as a function of λ. Squares with error bars and black solid line correspond to the experimental and simulated results, respectively. 48

Figure 5.6 Measured optical transmission as a function of time t for λ = 1.55 μm, when V_{dc} is switched on and off for (a) VO_2/TiO_2- and (b) $VO_2/SnO_2/TiO_2$-based devices. The magnitude of transmission is also expressed in color from yellow (low transmission) to red (high

transmission). Black solid lines are the fitted results with the formula of $1 - \exp(-t/\tau)$ and $\exp(-t/\tau)$........ 50

Figure B.1 70 degree tilted SEM image for the etching profile of VO_2on SnO_2/ TiO_2 by ICP with Cl_2/Ar........ 64

Figure B.2 Microscopic image of the etched VO_2 on SnO_2/ TiO_2 by RIE with CF_4. The inset illustration shows the 3D structure of the sample........ 65

Figure B.3 Thickness change of diluted Su-8 2000.5 as a function of the fraction in a mixture of Su-8/ cyclopentanone. The su-8 mixture is spin-coated with 5500 rpm........ 68

Figure B.4 Microscopic image of the Si NM transfer printed VO_2 on SnO_2/ TiO_2. The inset illustration shows the 3D structure of the sample........ 68

Figure B.5 Microscopic image of the 700 nm width SiO_2 etching mask on the Si NM. The inset illustration shows the 3D structure of the sample........ 70

Figure B.6 Microscopic image of the Si-VO2 integrated optical switch. The distance between metal electrodes of 5 μm was defined by e-beam lithography. The inset illustration shows the 3D structure of the sample........ 71

List of Tables

Table 1.1 Comparison of electrical and optical properties for phase transition materials. ……..2

Table 3.1 A comparison of extracted device model parameters for thermally triggered VO_2 RF switches at the ON- and OFF- states. …………………………………………………………23

Table 4.1 A comparison of extracted device model parameters for electrically triggered VO_2 RF switches at the ON- and OFF- states. …………………………………………………………35

Table A.1. The refractive index *n* and extinction coefficient *k* as a function of temperature at the fixed telecommunication wavelengths of 1310 nm and 1550 nm . ……………………………..55

Table A.2. The refractive index *n* and extinction coefficient *k* as a function of wavelength at room temperature (298 K) and high temperature (373 K) . ……………………………………58

1. Introduction

1.1. Correlated oxide materials

Correlated oxide materials have been studied for their interesting physical/chemical phase transition mechanism accompanied by dynamic changes in properties such as high-temperature superconductivity[1], and colossal magnetoresistance[2]. Among those correlated oxide materials, vanadium dioxide (VO_2) is one of the most fascinating and most studied materials due to several reasons. Firstly, compared to other correlated oxide materials that have a lower or much higher phase transition temperature than room temperature, the bulk VO_2 exhibits a sharp insulator-to-metal phase transition (IMT) at 341 K (68 °C)[3], which is slightly above the room temperature and enables us to utilize the transition characteristic for practical application devices. Secondly, since the electrical resistivity of the bulk VO_2 changes by 4~5 orders of magnitude during the IMT[4, 5], the VO_2 is a promising material candidate for electrical devices. Thirdly, dramatic changes in optical constants (Δn~1.4, Δk~2.7 at 1550 nm wavelength) of the VO_2 make it suitable for optical applications[6]. Lastly, the phase transition of the VO_2 can be triggered by many different excitation methods including temperature change[3] or optical pumping[7] or electric fieldand current injection[8], which broadens the applications. Table 1.1 shows the comparison of electrical and optical properties of phase transition materials whose phase transition temperature is close to room temperature. For $NdNiO_3$, the phase transition temperature is below the room temperature. Although many studies have demonstrated cooling devices in recent years[9-11], cooling devices are still considered to be much challenging than heating. The phase transition

temperature of VO_2 is above the room temperature but lower than the other materials, which makes it much easier to utilize phase transition characteristics with lower power consumption. With such novel properties of the VO_2, many application devices have been reported including Mott transistors[12], memristers[13, 14], and optical modulators[15-17]

Table 1.1 Comparison of electrical and optical properties for phase change materials.

Materials	Phase Change Temperature (K)	Resistivity change ratio (*R/R*)	Refractive index change (*Δn*)	References
$NdNiO_3$	~200	$\sim10^3$	~0	18, 19
VO_2	~341	$\sim10^5$	~1.4	6
$SmNiO_3$	~ 403	$\sim10^1$	~1.5	20, 21
GeSbTe	~413	$\sim10^4$	~2.85	22, 23

1.2. Phase transition mechanism of VO_2

The bulk VO_2 exhibits a sharp insulator-to-metal phase transition (IMT) from the monoclinic insulating phase to the tetragonal metallic phase at 341 K (68 °C). The Mott-Hubbard model has served for decades to explain correlated oxide phase transition including the VO_2[3, 24, 25]. The resistivity of the VO_2 changes 4 to 5 orders of magnitude due to the change of number of carriers, not the carrier mobility. Fig. 1.1 (a) shows the cross-sectional view of the VO_2 crystal structure. The VO_2 below the transition temperature is in insulating phase with a monoclinic tilt of rutile structure. The structure involves the pairing of vanadium atoms (V-V bonding) and off-axis displacement of them. At around 341 K, slightly above the room temperature, the VO_2 undergoes structural phase transition (SPT) and becomes metallic phase with a rutile tetragonal structure.

The vanadium atoms in this phase are positioned at the center of an oxygen octahedron. Therefore, the insulator-to-metal phase transition is basically the consequence of the displacement of vanadium atom.

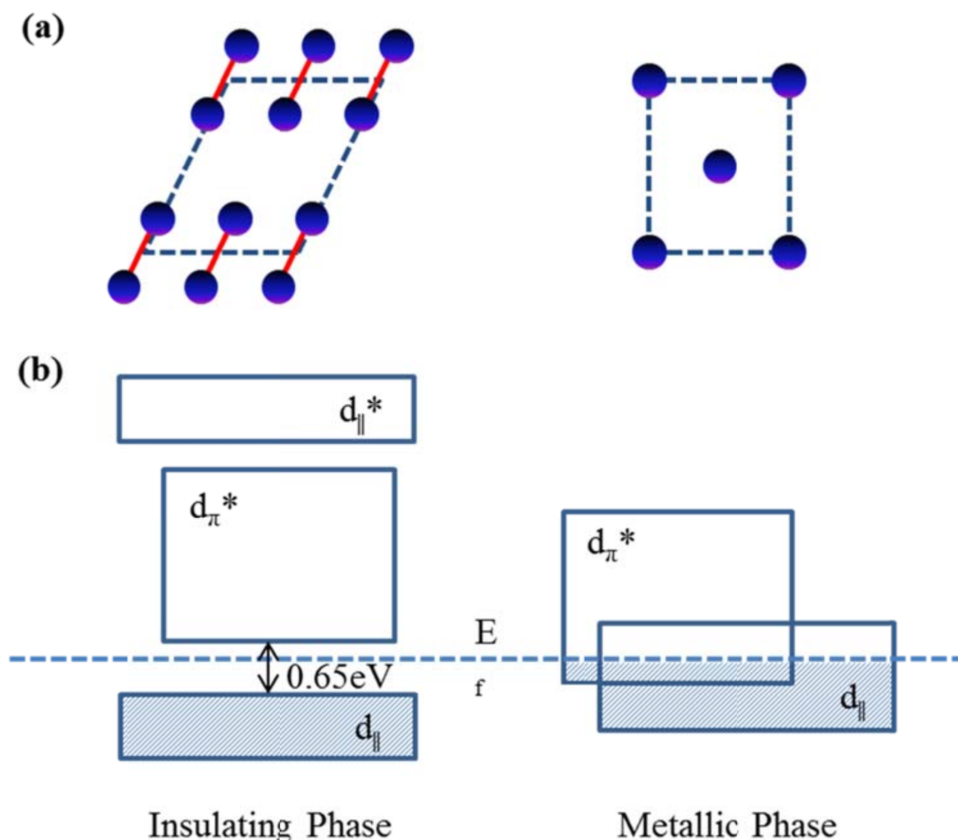

Figure 1.1 Schematic lattice structure and band diagram of VO_2 for insulating and metallic phase. **(a)** Cross-sectional view of crystal lattice structure change of VO_2. **(b)** Band diagram change of 3d bands near the Fermi level for VO_2**.**

Along with the SPT, IMT in VO_2 occurs and band structure also changes as shown in Fig. 1.1 (b). In the insulating phase, the distortion in the crystal structure shortens V-O distance. This destabilizing π* orbital so that the π* bands are raised above the Fermi energy level. Also, all d

level orbitals split into bonding-antibonding components, which results in the upward shifting of both π* band and upper half of $d_{||}$ band. Band structure in the metallic phase can be explained based on the conventional band theory. The levels in octahedral crystal field are split into π* and $d_{||}$, which have electron states near the Fermi energy level and make the metallic state.

Here the phase transition mechanism is described using the Mott-Hubbard model. However, the mechanism of the VO_2 phase transition is still unclear whether it is the Peierls type or the Mott-Hubbard type[25]. If SPT induces IMT, the mechanism is the Peierls type. However, if it is inverse order, the mechanism is the Mott-Hubbard type.

1.3. Growth of highly epitaxial VO_2 thin films

VO_2 is one of the most studied correlated oxide material because in the single crystalline bulk VO_2, the phase transition temperature is slightly above room temperature, sharp resistivity change occurs within a few 0.1 K temperature change, and resistivity change $\Delta\rho/\rho$ exceeds more than 4 orders of magnitude. Up to date, however, the imperfect crystal quality of VO_2 films has limited the development of high-performance VO_2-based devices. Since small dimension geometry such as thin film is essential for most of practical device applications, developing high quality VO_2 films has been a critical challenge.

A single crystalline bulk VO_2 or epitaxial VO_2 thin film has commonly suffered from the fracture and degradation of their physical properties due to a large elastic stress during phase transition[26-28]. For example, an attempt to grow high quality VO_2 thin film on TiO_2 single crystalline substrate was unsuccessful because the misfit strain in the VO_2 film lowered the phase transition temperature down to ~290 K[28]. Such low-temperature phase transition is inapplicable

for devices operating at room temperature. Also, when thick VO_2 films are grown, the VO_2 films crack as the phase transitions are repeated because of a large stress during the SPT. Due to such difficulties in VO_2 growth, polycrystalline or amorphous VO_2 thin films have been alternatively used for device applications[15, 29, 30].

In this work, high performance VO_2 device applications are demonstrated using breakthrough highly epitaxial VO_2 thin films, which are grown on TiO_2 (001) substrate with a SnO_2 buffer layer by pulsed laser deposition (PLD). SnO_2 is an ideal template for growing epitaxial VO_2 because it is insulating and has rutile symmetry. Particularly, the SnO_2 template is adopted because of its large lattice mismatch with VO_2, contrary to conventional thin-film epitaxy that prefers a lattice-matched substrate or template. The huge lattice mismatch (i.e., ~4.2 %) between VO_2 and SnO_2 would lead to an incoherent interface with abrupt strain relaxation and uniform bulk-like lattices in VO_2 films, relieving the lattice constraint imposed by the substrate. These conditions are essential for realizing the sharp and homogeneous IMT dynamics. The details on VO_2 growth can be found elsewhere[6].

The epitaxially grown VO_2 film was examined by using a high-resolution four-circle X-ray diffraction (XRD) machine (Bruker D8 advance). Fig. 1.2 presents phi (φ) scan of the VO_2 film on TiO_2 (001) substrate with SnO_2 buffer layer. Four diffraction peaks with 90 ˚ spacing confirm the four-fold symmetry structure of single crystalline VO_2. Additionally, the well-aligned diffraction peaks and the full width at half maximum (FWHM) value of ~0.8 ˚ confirm the high quality epitaxially grown VO_2 film with the in-plane crystallographic orientation of $[100]_{R_VO_2}//[100]_{SnO_2}//[100]_{TiO_2}$. This unique bilayer platform of SnO_2/TiO_2 allowed us to achieve crack-free epitaxial VO_2 thin films with homogeneous bulk-like lattices.

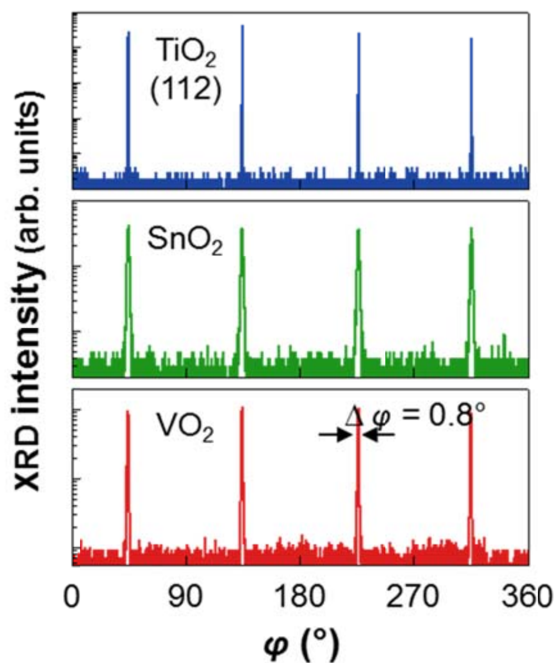

Figure 1.2 XRD φ scan of the off-axis (112) reflections of (top) TiO_2, (center) SnO_2, and (bottom) VO_2, clearly indicating the epitaxial growth of VO_2

1.4. Thesis organization

In this thesis, previous works on VO_2 are briefly reviewed and the electrical and optical properties of newly developed epitaxial VO_2 on SnO_2/TiO_2 are described. In addition, the novelties of epitaxial VO_2 are discussed and the demonstrations of electrical/optical application devices based on epitaxial VO_2 are presented.

Chapter 2 covers the properties of epitaxial VO_2 on SnO_2/TiO_2, which were used in subsequent chapters for device design and characterization. The novelties of epitaxial VO_2 compared to poly crystalline VO_2 are also discussed. Chapter 3 describes the demonstration of thermally triggered

RF switches based on the epitaxial VO_2. The conventional RF switch techniques and other thermally triggered RF switches were reviewed. Chapter 4 describes the realization of electrically triggered RF switches based on the epitaxial VO_2. Chapter 5 describes the realization of electrically triggered optical switches based on the epitaxial VO_2. To fully utilize the properties of VO_2, Si- VO_2 integrated structure was employed. Chapter 6 presents a summary of this thesis. Appendix shows measured optical constants for the epitaxial VO_2 as a function of temperature and wavelength. The detailed fabrication process for the Si- VO_2 integrated optical switches is also discussed.

2. Properties of VO_2

The simplest way to trigger the phase transition in VO_2 is to elevate temperature above 341 K. IMT in VO_2 is accompanied by a sharp and large change in resistivity of the material. Bulk single crystalline VO_2 is reported to exhibit 4~5 orders of magnitude during IMT[4, 5]. Temperature dependent phase transition is a reversible process. At metallic state, by lowering temperature leads to metal-to-insulator phase transition (MIT). Due to the hysteresis in VO_2, MIT temperature is always lower than IMT temperature.

2.1. Phase transition property changes by growth conditions

For VO_2 thin films, phase transition properties change by the growth conditions such as deposition method, pressure, temperature, and substrate material. Fig. 2.1 shows issues associated with different growth conditions for the VO2 thin films. Fig. 2.1 (a) presents VO_2 films grown on Si/SiO_2 substrate by precursor oxidation process and pulsed laser deposition, which have hysteresis loop gap $\Delta T=7$ K and 10 K, respectively[31]. Large hysteresis gap can be useful for memory device applications but can lower the switching speed. Fig. 2.1 (b) shows a study that epitaxial VO_2 films on (100) TiO_2 substrate experience a large uniaxial tensile strain[32]. The strain results in cracks on the VO_2 films and IMT temperature can be increased up to 365 K by engineering the strain. Also, cracks on the VO_2 films can cause reliability issues for application devices. Fig. 2.1 (c) shows VO_2 films grown on Si and Ge substrate by RF sputtering[33]. The resistivity change of the VO_2 on Si is less than two orders of magnitude, while

that of the VO_2 on Ge is about three orders of magnitude. It should be noted that larger resistivity change for the VO_2 on Ge is still one order smaller than that of single crystalline bulk VO_2. Fig. 2.1 (d) shows the resistivity change ratio depending on the growth methods[34]. Most of VO_2 films show smaller resistivity change as the thickness decreases.

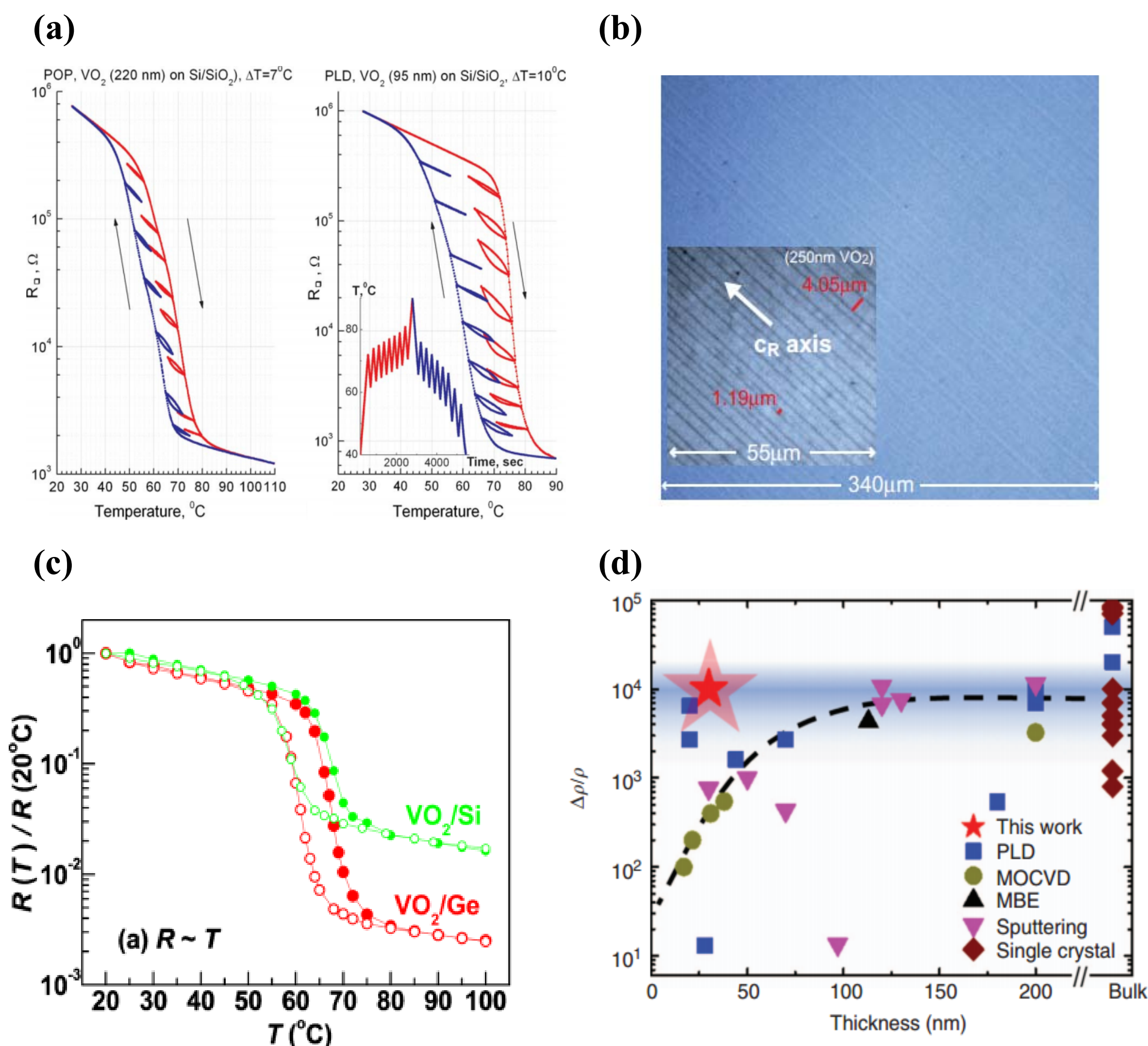

Figure 2.1 Issues for VO_2 thin films associated with different growth conditions. **(a)** Hysteresis loop gap change by growth method[31]. **(b)** Cracks due to the large tensile strain in the films[32]. **(c)** Resistance change ratio difference depending on substrate[33]. **(d)** Resistivity change ratio difference depending on growth methods[34].

2.2. Electrical properties of epitaxial VO_2

The newly developed $VO_2/SnO_2/TiO_2$ film shows sharp and homogeneous SPT, as well as sharp IMT. The phase transition in epitaxial VO_2 films is characterized by measuring the electrical resistivity in vacuum as a function of temperature for the samples with or without SnO_2 template (Fig. 2.2). The measured IMT showed resistivity change by a factor of ~10^4 in $VO_2/SnO_2/TiO_2$ film, which is comparable to single crystalline bulk VO_2. On the other hand, it became suppressed in VO_2/TiO_2 film due to the presence of strain gradient and cracks. Also, $VO_2/SnO_2/TiO_2$ film showed sharp phase transition, whose transition width ΔT (measured as FWHM of the logarithmic derivative of the resistivity with temperature) was as small as ~0.8 K[6].

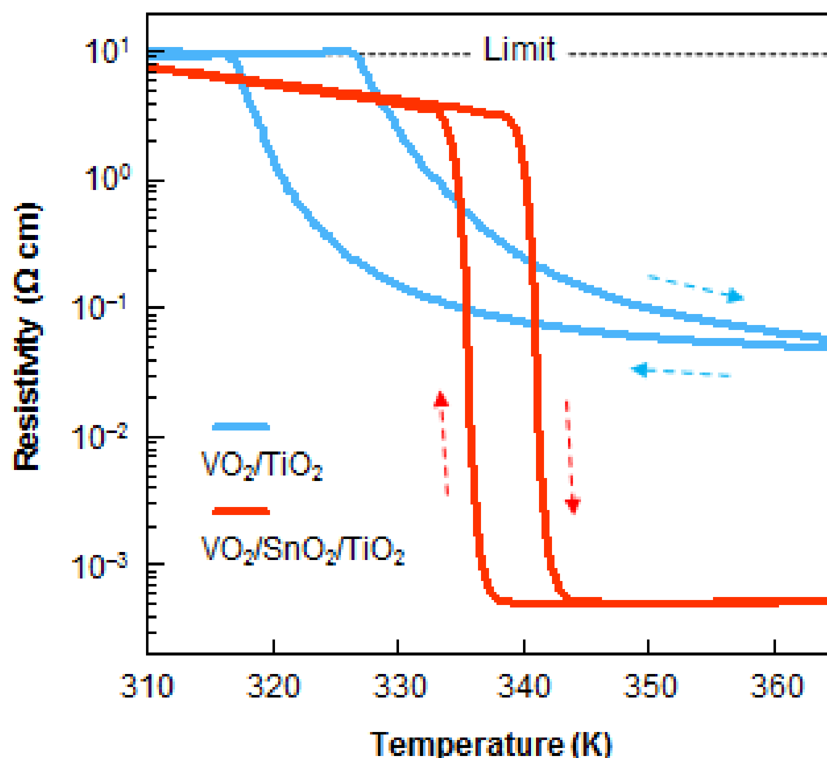

Figure 2.2 Electrical resistivity for VO2 films as a function of temperature.

Hysteresis loop gap for $VO_2/SnO_2/TiO_2$ film was as narrow as ~ 5 K, which confirms high film quality. In the metallic phase, our $VO_2/SnO_2/TiO_2$ film showed not only the small resistivity, but also a clear metallic characteristic (i.e., decrease in resistivity with decreasing temperature), owing to the absence of severe structural/chemical defects in the film. These results confirmed the excellent phase transition features in SnO_2-templated epitaxial VO_2 films.

2.3. Optical properties of epitaxial VO_2

The phase transition of VO_2 is accompanied by optical constants change. Using spectroscopic ellipsometry (J.A. Woollam M-2000 ellipsometer) and temperature controlled stage (Bioscience tools temperature controller), the refractive index n and extinction coefficient k are measured as a function of temperature. Ellipsometry data was obtained by repeating measurement 4 times with changing beam angles from 60 to 75 degree for the near infrared wavelength range of 900 nm to 1650 nm. This wavelength range covers most widely used wavelengths for telecommunication applications. The sample temperature was swept from 298 K to 353 K for every 1 degree with 0.1 K resolutions.

Fig. 2.3 shows the optical constants, n and k values, measured during IMT, as functions of temperature and the wavelength λ of incident light for 300-nm-thick VO_2 films. Fig. 2.3 (a) and (c) are optical constants for $VO_2/SnO_2/TiO_2$ film, while Figure 2.3 (b) and (d) are for VO_2/ TiO_2 film. By comparing measurement results from two different structures, for the VO_2 film on bare TiO_2 substrate, the n and k exhibited gradual change across IMT. On the other hand, for the VO_2 film on SnO_2-templated TiO_2, the n showed abrupt change for every λ across IMT.

In Fig. 2.4, dynamic changes of n and k values are shown as a function of temperature for wavelengths of 1310 and 1550 nm. Optical constants change confirms sharp phase transition

near 341 K. At 1550nm, n values change from 3.10 to 1.74 and k values change from 0.30 to 2.98 for 298 K and 353 K, respectively. Considering refractive index step, Δn, is a few 10^{-3} for typical silicon based optical modulator[35], Δn of ~1.4 in VO_2 during phase transition is much larger and this optical property can be used for variety of optical applications.

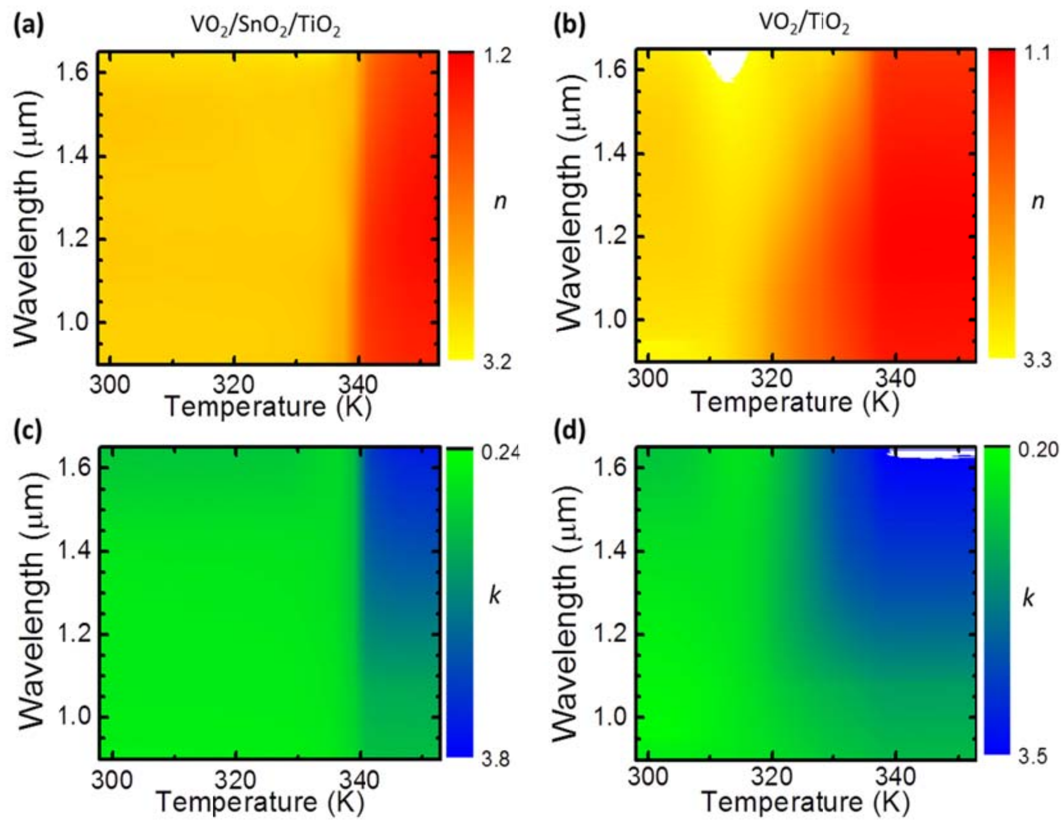

Figure 2.3 Optical constants change during IMT in VO_2 film. **(a), (b)** Refractive index n as functions of T and wavelength λ for 300-nm-thick VO_2 films on TiO_2 (a) and SnO_2/TiO_2 (b). **(c), (d)** Extinction coefficient k as functions of T and wavelength λ for 300-nm-thick VO_2 films on TiO_2 (c) and SnO_2/TiO_2 (d).

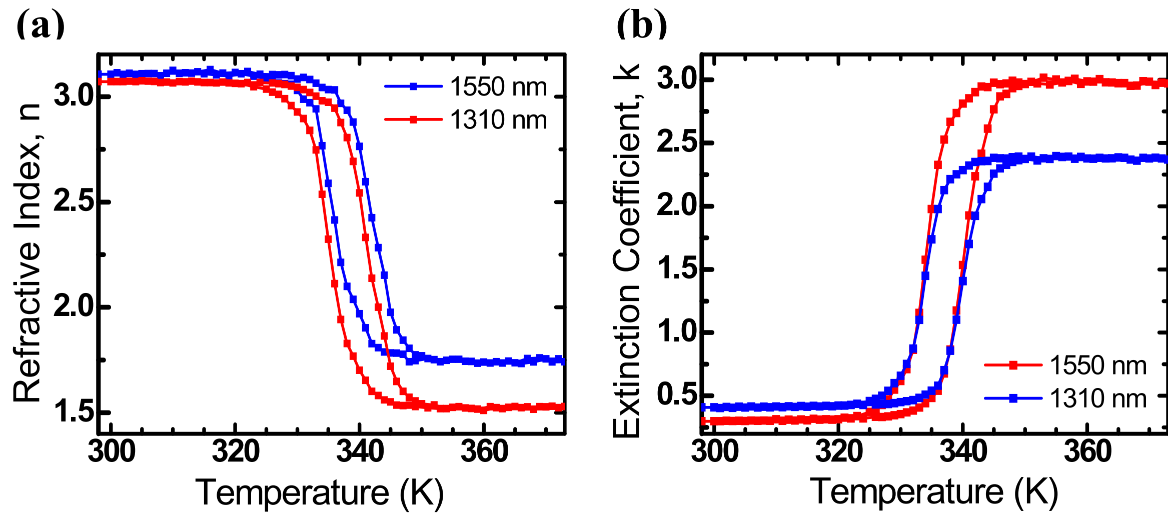

Figure 2.4 Optical constants of VO_2 on SnO_2/TiO_2 for telecommunication wavelengths, 1310 and 1550 nm. (a) Refractive index, *n*. (b) Extinction coefficient, *k*.

.

3. Epitaxial VO_2-based RF Switches with Thermal Excitation

In this chapter, thermally triggered radio-frequency (RF) switches based on epitaxial vanadium dioxide (VO_2) thin films are demonstrated. Utilizing the SnO_2 template, high-quality VO_2 thin film was epitaxially grown on TiO_2 (001) substrate. Fast insulator-to-metal phase transition at low temperature allowed VO_2 RF switches to exhibit sharp changes in the RF insertion loss greater than 15 dB at 333 K and 339 K during cooling and heating. VO_2 RF switches also completed the transition of S_{21} less than 3 K and showed a low loss operation frequency of up to 24.2 GHz with a low insertion loss of -1.36 dB and isolation of 17.56 dB at 12.03 GHz, respectively. The demonstration suggests that epitaxial VO_2-based RF switches can be used in switching elements up to Ku-band RF switch circuits.

3.1. Conventional RF switches

Radio frequency (RF) switches are devices to control high frequency signals through transmission lines and widely used for signal routing in wireless systems. By using the RF switches, not only the signals can be turned on and off, but also the RF switches in a matrix configuration can route the signals from multiple inputs to multiple outputs.

The conventional RF switches are classified into two categories of electromechanical and solid-state switches[36]. The electromechanical type switches employ micro-electro-mechanical system

(MEMS) system[37-41] and the solid-state type does p-i-n junction diodes[42, 43] and filed effect transistor (FET)[44, 45]. Fig. 3.1 shows conventional RF switches including solid-state RF switch with GaN based heterojunction field-effect transistor (HFET) and MEMS RF switch with aluminum (Al) membrane.

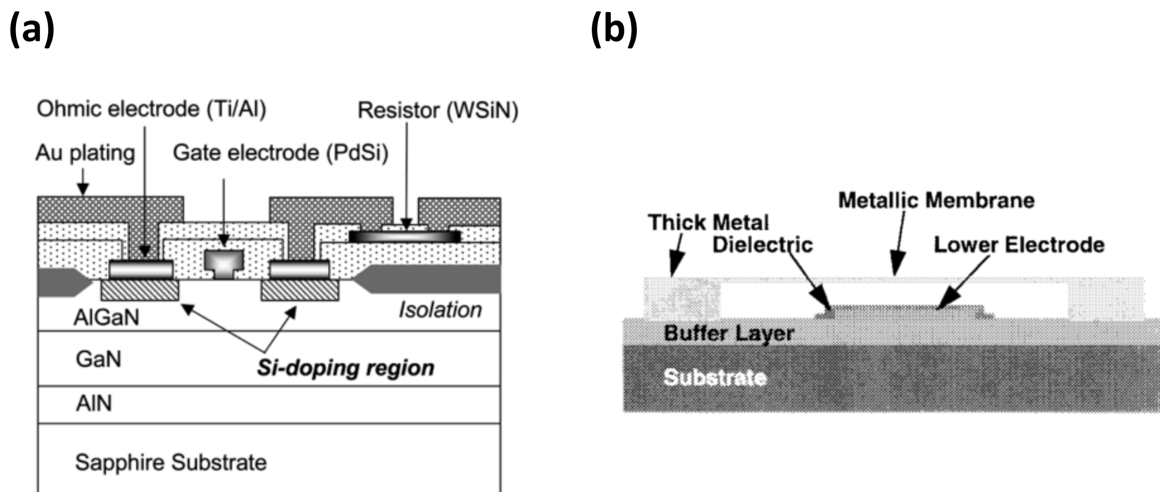

Figure 3.1 Schematic cross section of conventional RF switches. **(a)** GaN based HFET solid-state RF switch[44]. **(b)** Al membrane based capacitive MEMS RF switch[40].

The p-i-n diodes type were the first extensively used RF switches in 1950s and are still being used today. Although p-i-n diode type RF switches have advanced over time, they also have limitations[46]. This type required a constant DC bias to keep ON-state and a high reverse voltage to switch off by making reverse bias mode diodes. Biasing the diodes was also difficult because the bias had to be applied through the RF signal transmission line, which results in bandwidth reduction and high loss. Therefore, another approach, FET type RF switches were proposed in 1980s. FET based RF switches show advantages over diode based ones such as a low power

consumption, a high switching speed, and isolated control voltage from signal path. However, they also have drawbacks including high cost and circuit design difficulties.

The first MEMS type RF switches were introduced in 1970s but they are still considered be immature because it was difficult to develop commercial fabrication technologies due to the structural complexity of the MEMS devices[37]. They have several more problems such as long-term reliability, low contact force for metal-to-metal contacts, and high power switching capability. However, the MEMS RF switches have clear advantages over solid-state type RF switches. MEMS switches have much lower ON-state insertion loss and high OFF-state isolation. There are represented by ON-state intrinsic resistance, R_{on}, and OFF-state capacitance, C_{off}, which directly affect cutoff frequency, F_{co}. Thus, F_{co} of MEMS type switches is improved at least several orders of magnitude compared to p-i-n type. MEMS type switches also suffer much less from intermodulation distortion due to the nature of mechanical switching mechanism.

3.2. Previous RF switches based on phase change materials

Alternative way to operate RF switches, using phase change materials, is proposed in 2000s. Phase change material switches have lower ON-state resistance for a same size device compared to MEMS switches[47] and lower OFF-state capacitance compared to solid-state switches[48]. Particularly, the device structure and fabrication of phase change material switches can be much simplified without having a typical p-i-n junction or mechanical structure. Also, they can be designed to consume zero power for steady state operation.

The phase change materials show large resistance change depending on temperature and by inserting these materials between metal transmission lines switching operation can be realized.

The phase transition can be triggered by heating the materials above the transition temperature by using hot probes[47], using lasers[49], direct heating by current injection[50], and indirect heating by using heater layer in the devices[51].

Besides VO_2, one of the most studied phase change materials studied for RF switch applications is germanium telluride (GeTe)[48, 52-54]. GeTe is attractive candidate since it exhibits the lowest ON-state resistivity amongst phase change materials[52].it is reported that this material showed the resistivity change of 7 orders of magnitude during the phase transition. However, the transition temperature is relatively high, ~ 463 K. VO_2 RF switches can operate under a lower transition temperature with reduced power consumption, compared with other thermally triggered RF switches[48, 55]. Fig 3.2 shows the schematic cross section of the RF switch based on GeTe. The thin film resistor layer was inserted below the phase change material to heat the GeTe and trigger the phase transition. At the room temperature GeTe is amorphous and in insulator phase, while above the phase transition temperature, GeTe becomes crystalline and metallic phase.

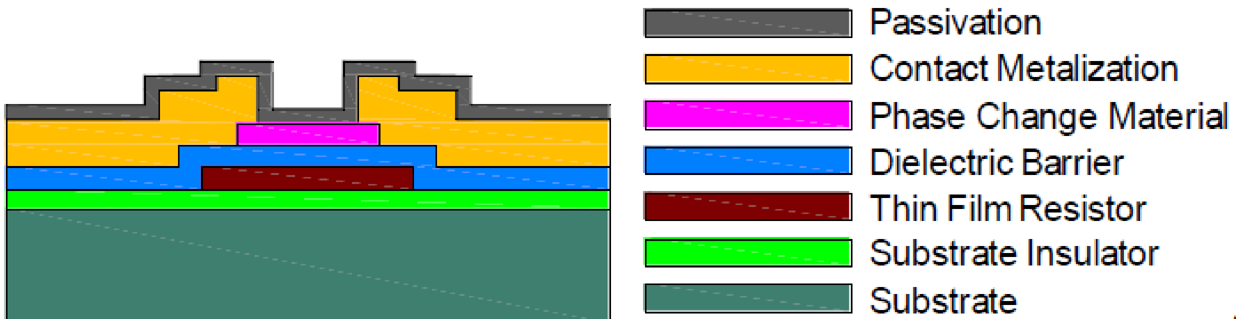

Figure 3.2 Schematic cross section of RF switch based on phase change material, GeTe[54].

3.3. Device design and fabrication

The high quality epitaxial VO_2 thin film was employed to fabricate the simple single-pole single-throw (SPST) type switches which use the change in RF impedance by heating and cooling. The RF switching and power characteristics were measured under various temperatures and demonstrated sharp resistivity changes, with the scattering (S-) parameter S_{21} greater than 15 dB at 333 K and 339 K, when switches were heated up and cooled down, respectively. VO_2 RF switches also completed the transition of S_{21} within 3 K of the IMT temperature and showed a low loss operation frequency of up to 24.2 GHz with a low insertion loss of -1.36 dB and isolation of 17.56 dB at 12.03 GHz, respectively.

The schematic illustration of the fabrication process is shown in Fig. 3.3 (a). The fabrication began with the epitaxial growth of the VO_2 thin-film on TiO_2 (001) substrate with a SnO_2 buffer layer by PLD (Fig 3.3 (a) i).Then, the coplanar waveguide (CPW) transmission line was patterned on top of the VO_2 layer (Fig 3.3 (a) ii), followed by the deposition of Ti/Au (10 nm/ 300 nm) metal stack by e-beam evaporation (Fig 3.3 (a) iii). Fig. 3.3 (b) shows a microscopic image of the finished CPW transmission line. The width of the signal line and the ground line were 54 μm and 133 μm with a 43 μm spacing and the length of the device was 140 μm, respectively. It should be noted that the device structure and pad design were optimized by using Keysight ADS 2013 momentum considering the complex EM effects including skin effect, substrate effect, and RF losses between each layer. The detailed design considerations will be discussed in the later section (the simulation part). A cross-sectional scanning electron microscope (SEM) image in Fig. 3.3 (c) shows 100 nm SnO_2 and 300 nm VO_2 layers.

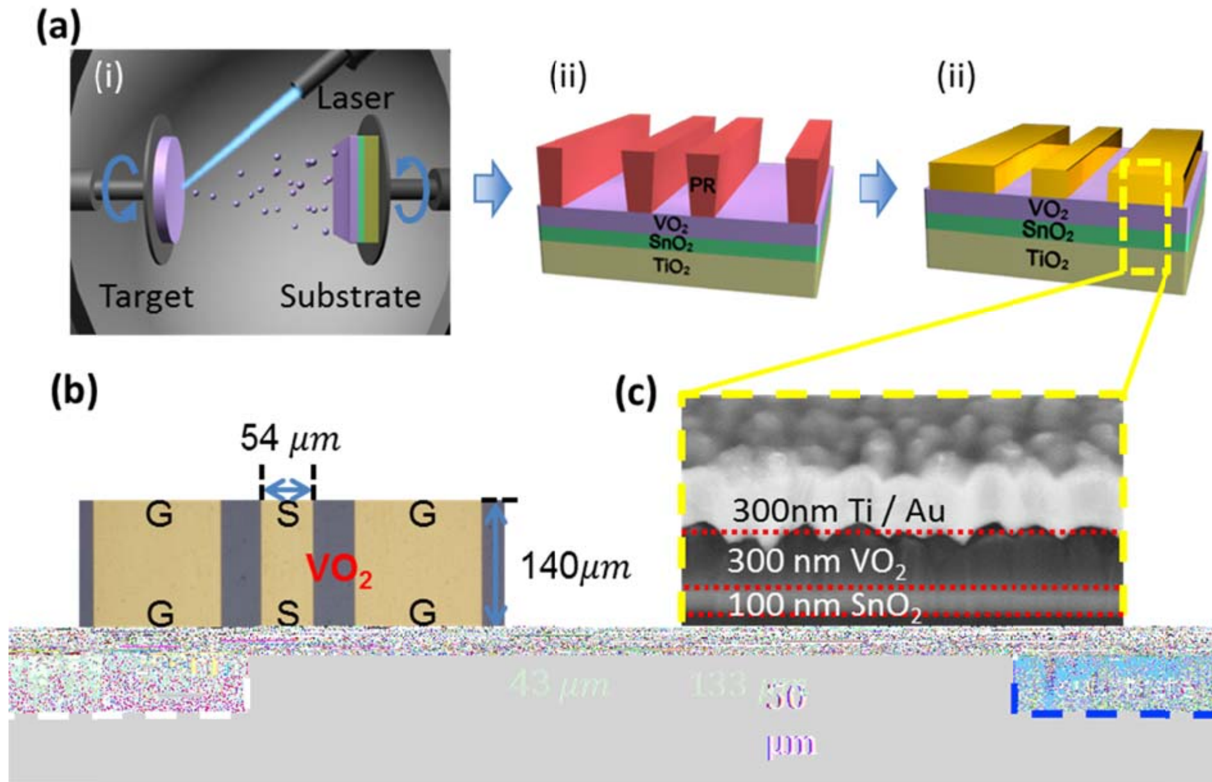

Figure 3.3 (a) A schematic illustration of the fabrication process for epitaxial VO_2 based RF switches. **(b)** A microscopic image of the device and its dimensions. **(c)** A cross-sectional scanning electron microscope (SEM) image of the finished device.

3.4. Device characterization

The switching characteristics of the fabricated VO_2 RF switches were measured by S-parameters under the frequency range from 45 MHz to 40 GHz using an Agilent E8364A performance network analyzer (PNA) with the heating stage to control the sample temperature. The temperature was carefully controlled from room temperature (298 K) to high temperature (363 K) with 1 K step during the measurement.

Fig. 3.4 (a) and (b) show the measured and simulated RF characteristics of VO_2 RF switches when the device was at the ON- and the OFF-states. In order to investigate the insertion loss and the transmission through the VO_2 RF switches, S_{11} and S_{21} were extracted. In Fig. 3.4 (a), the measured S_{11} and S_{21} show an operation frequency of up to 24.2 GHz at 298 K with relatively low RF losses, as low as -1.36 dB at 12.03 GHz and -2.32 dB at 18.02 GHz. The simulated operation frequency of 23.33 GHz also matches well with the experiment results. Fig. 3.4 (b) shows the RF characteristic above the phase transition temperature. Namely, the device was heated at 363 K, in order to make the VO_2 layer stay at the stable metallic state. At the metallic state, it is known that the resistivity of VO_2 decreases by 4~5 orders of magnitude[4, 5] which suppresses the transmission signal over the wide range of frequencies. At the OFF-state, S_{21} characteristics showed a similar low level of -16.49 dB at 45 MHz and -18.05 dB at 40 GHz. The simulated RF characteristics at the OFF-state also showed a similar low level as compared to the measured result, indicating that our model can be utilized for other types of the VO_2 RF switches. The group delay is one of the important parameters to evaluate the phase distortion by measuring the average travel time at a certain frequency signal to travel through the device under operation. Fig. 3.4 (c) shows the measured group delay of VO_2 RF switches at the ON-state. The spikes referring to the group delay ripples and the average delay represents the amount of time for a certain frequency signal to travel from the signal port to the ground port through the device under operation. The measured average delay is 2.49 ps, the highest group delay ripple is 32 ps, and the lowest value is -29 ps. The simulated average delay is 3.74 ps with 8.32 ps of the highest group delay ripple and 3.4 ps of the lowest value. The small group delay indicates that the VO_2 RF

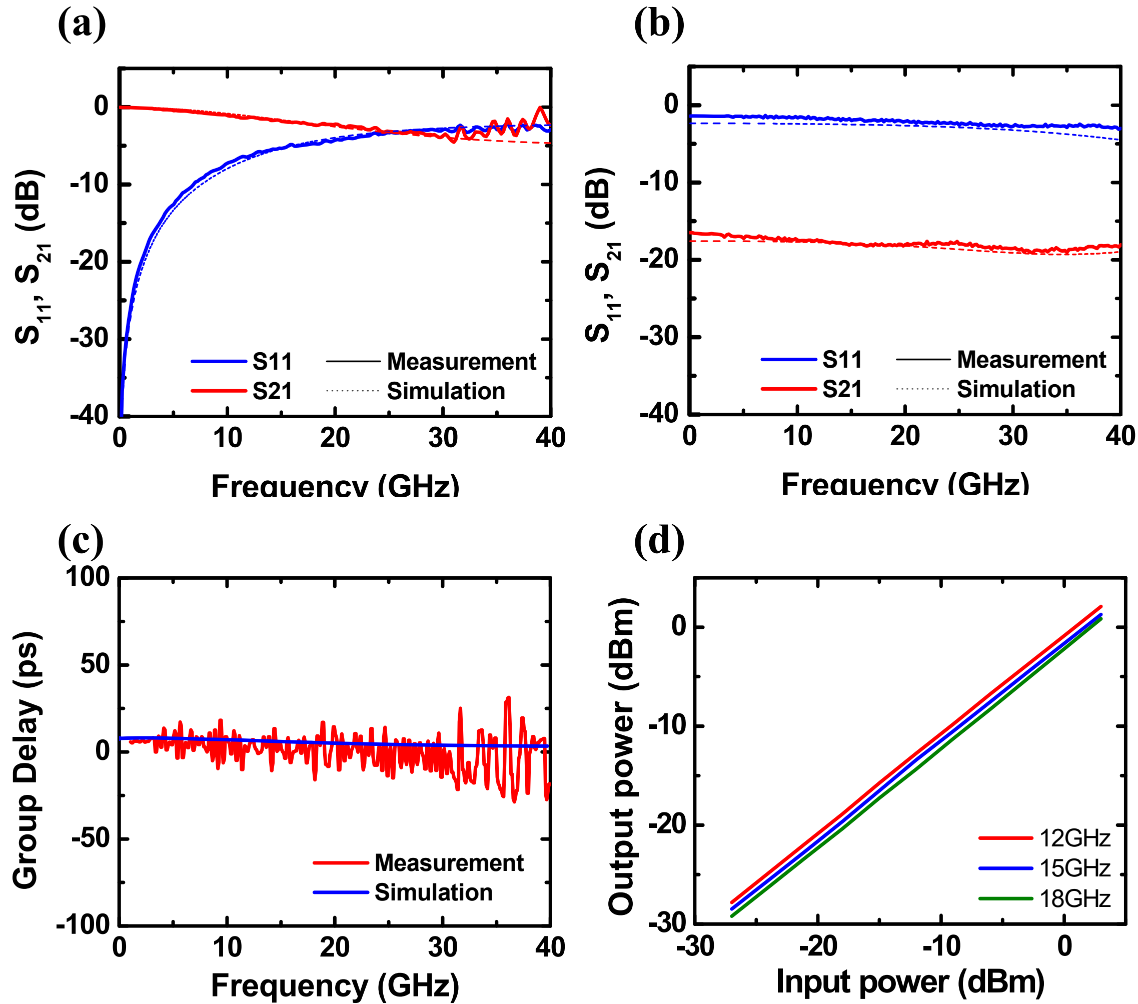

Figure 3.4 The measured and simulated S_{11} and S_{21} characteristics of VO_2 RF switches **(a)** at the ON-state, and **(b)** at the OFF-state under a frequency range of 45 MHz to 40 GHz. **(c)** The measured and simulated group delay of the device. **(d)** The output RF power as a function of input RF power from -27 dBm to 3 dbm for various frequency points.

switches were stable over the frequency range, making this device suitable for a switching element up to Ku-band RF switching circuits. In Fig. 3.4 (d), we measured output power as a function of input power for various frequencies in Ku-band (i.e., at 12 GHz, 15 GHz, and 18 GHz, respectively) at the ON-state. The power range from -27 dBm to 3 dBm from PNA was

used as an input power source and the signal was read through the spectrum analyzer (Agilent E4407B). VO_2 RF switches exhibit linear RF power characteristics and compression was not shown for the entire input power range at the ON-state. As the input signal frequency increases, output power decreases due to the insertion loss increase.

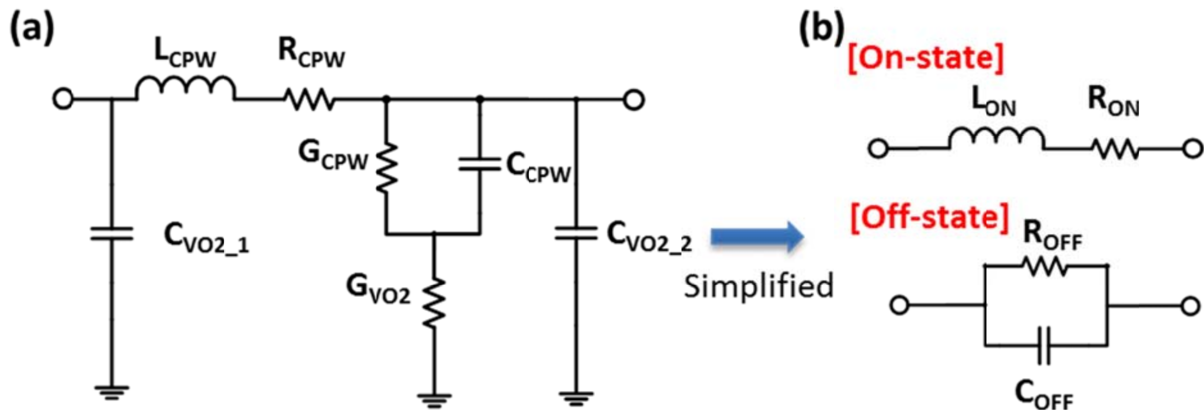

Figure 3.5 (a) An equivalent circuit model that was used to model VO_2 RF switches. **(b)** A simplified equivalent circuit model for the switch operation. At room temperature, the switch is at the ON-state and can be simplified to the RL series circuit. At above the IMT temperature, the switch is at the OFF-state and can be simplified to the RC parallel circuit.

When the dimensions of VO_2 RF switches were designed, the following factors were considered. Firstly, most of the TE filed is concentrated in the VO_2 layer, as the magnetic field in CPW is elliptically polarized. Secondly, since the VO_2 layer has a high dielectric constant (ε = 40.6 at 10Hz)[56], it effectively reduces radiation losses. Taken together, the optimized CPW structure can be used for high frequency signal switching devices with thermally controlled phase transition of VO_2. Fig. 3.5 (a) represents the equivalent circuit model that was used to model the VO_2 RF

switches to further analyze the switching mechanism[57-59]. Each component value of the equivalent circuit was obtained by curve fitting the measured S-parameters.

Components	298 K On (Insulator)	363 K Off (Metallic)
L_{CPW} (pH)	79	1650
R_{CPW} (Ω)	1.2	480
G_{CPW} (S)	800	200
C_{CPW} (fF)	180	3
G_{VO2} (S)	2.5×10^{-5}	2.5×10^{-1}
C_{VO2_1} (fF)	30	2
C_{VO2_2} (fF)	30	2

Table 3.1 A comparison of extracted device model parameters for thermally triggered VO_2 RF switches at the ON- and OFF- states.

Shown in Table 3.1 are the equivalent component values of VO_2 RF switches at the ON- and OFF-states. The L_{CPW}, R_{CPW}, G_{CPW}, and C_{CPW} values in Table I refer to the equivalent components of the loss CPW line. The VO_2 layer is represented as G_{VO2} for the real part of the loss, and C_{VO2_1} and C_{VO2_2} for the imaginary part of the loss. When VO_2 RF switches operate at the ON-state, RF signal can be transmitted with the low real part insertion loss (R_{CPW}) as low as 1.2Ω. On the other hand, when VO_2 RF switches operate at the OFF-state above phase transition temperature, the VO_2 layer becomes the metallic phase with nearly 4 orders[6] of magnitude lower resistance and thus VO_2 RF switches behave as an attenuator. The reduced resistance of the VO_2 layer at the OFF-state becomes a dominant loss part with the series of real losses of CPW line components. As a result, the R_{CPW} increases to 480 Ω, which effectively attenuates the signal.

Based on the equivalent circuits, the figure of merit of RF switch, the cut-off frequency (F_{co}), is calculated based on the following equation (1)[60],

$$F_{co} = \frac{1}{2\pi R_{on} C_{off}} \quad (1)$$

where, R_{on} and C_{off} are the resistance at the ON-state and the capacitance at the OFF-state, respectively. In this calculation, an R_{on} of 1.2 Ω and C_{off} of 7×10^{-15} F were used and yielded a F_{co} value of 18.9 THz which is higher than that of typical p-i-n diodes, FET switches,[38] and other reported phase change material switches[52].

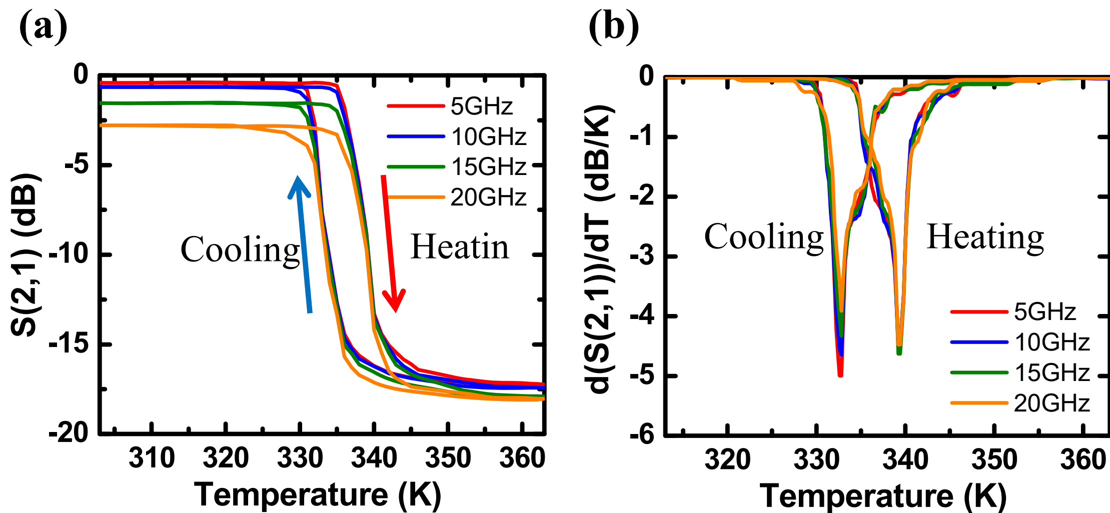

Figure 3.6 (a) S_{21} curves for VO_2 RF switches under the heating and the cooling cycles by thermally triggered IMT. **(b)** Derivatives of S_{21} curve, d(S_{21})/dT to show the peaks and FWHM of IMT curves.

The S_{21} value as a function of temperature in the range from room temperature to 363 K is shown in Fig. 3.6 (a). VO_2 RF switches were heated and cooled at various frequency points (namely, 5,

10, 15, and 20 GHz) to investigate the IMT point. For all frequencies, transitions in S_{21} for both heating and cooling sequences occurred at the same temperature, which is the same transition temperature as the resistivity change. In order to further analyze the phase transition characteristic, the derivative of S_{21} is plotted in Fig. 3.6 (b). IMT points for heating and cooling cycles can be clearly observed at 339 K and 333 K, respectively, with the 6 K hysteresis loop gap in all frequency ranges. The S_{21} based full width at half maximum (FWHM) of IMT is less than 3 K for both heating and cooling cycle, which confirms that IMT in this structure exhibits a similar sharp transition property to that of the bulk sample[6]. However, the 3 K transition value based on S_{21} is still wider than the resistivity-based FWHM value[6]. While resistivity transition only involves the DC component of the VO_2 layer, the transition based on S_{21} (i.e., a phase transition in the microwave regime) involves parasitic capacitance of the VO_2 layer and thus results in a wider transition temperature.

3.5. Summary

In Summary, we demonstrated thermally triggered RF switches based on epitaxial VO_2 thin film with the simple device structure. The high quality epitaxial VO_2 thin film was achieved by using the SnO_2 template layer in between the VO_2 layer and TiO_2 substrate, which performed a similarly sharp phase transition to that of the bulk VO_2. Fast insulator-to-metal phase transition at a low temperature allowed VO_2 RF switches to exhibit sharp resistivity changes with the S_{21} change greater than 15 dB at 333 K and 339 K when switches were heated up and cooled down, respectively. VO_2 RF switches performed the sharp transition of S_{21} less than 3 K and showed a low loss operation frequency up to 24.2 GHz with a low insertion loss of -1.36 dB and isolation

of 17.56 dB at 12.03 GHz. The demonstration suggests that PLD-grown VO_2 based RF switches can be used in switching elements up to Ku-band RF switch circuits.

4. Epitaxial VO_2 based RF Switches with Electrical Excitation

In this chapter, electrically triggered phase transition of epitaxial VO_2 and RF switches are demonstrated. Highly epitaxial VO_2 and SnO_2 template layer was grown on TiO_2 (001) substrate by pulsed laser deposition. The 4 orders of resistance change of the VO_2 thin films was achieved with relatively low threshold voltage for IMT phase transition as low as 13 V. VO_2 RF switches also showed high frequency responses of insertion losses of -3 dB at the ON-state and return losses of -4.3 dB at the OFF-state over 27 GHz. Furthermore, it is expected to perform intrinsic cut-off frequency of 17.4 THz. The study on electrical IMT dynamics revealed 840 ns of phase transition time.

4.1. Previous electrically triggered RF switches based on VO_2

The phase transition of VO_2 can be triggered by many different types of stimulations but electrical excitations by applying voltage bias or current injection were of particular interest. By using electrical excitation, conventional concepts for electronic devices are applicable and this opens up applications for electrical switching devices, memory devices, and communication devices.

In the last decade, a few studies on RF switches based on VO_2 were reported[29, 30]. They used poly crystalline VO_2 grown on single crystalline sapphire (Al_2O_3). Although they exhibit reasonable

RF performance, phase transition characteristics were much degraded compared to single crystalline bulk VO_2. As shown in Fig 4.1, their phase transition took > 30 K by heating and resistivity change by electrical phase transition was 3 orders of magnitude.

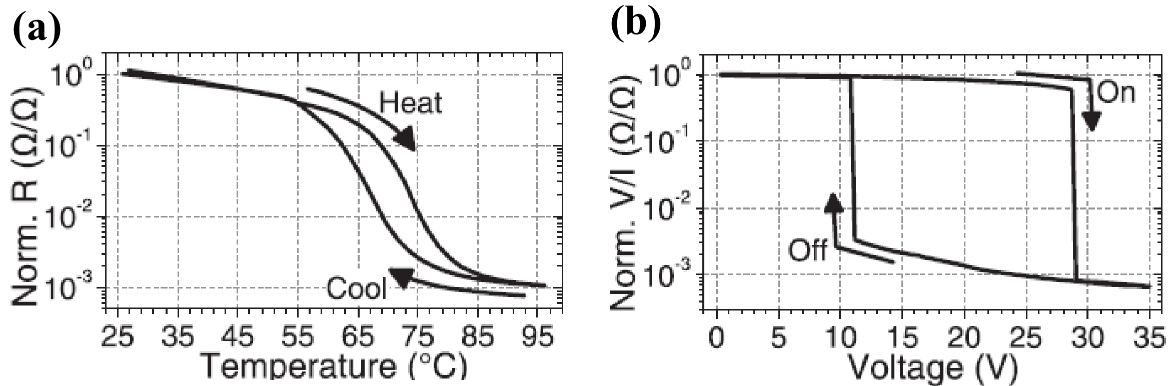

Figure 4.1 Phase transition characteristics of poly crystalline VO_2 on single crystalline sapphire substrate[29]. **(a)** The resistivity as a function of temperature by thermal phase transition. **(b)** The resistivity change as a function of voltage.

4.2. Device design and fabrication

In this chapter, electrically triggered RF switches were demonstrated using a highly epitaxial VO_2 thin films, grown on TiO_2 (001) substrate with SnO_2 template layer by pulsed laser deposition (PLD). This unique bilayer platform of SnO_2/TiO_2 allowed us to achieve crack-free epitaxial VO_2 thin films with homogeneous bulk-like lattices. As a result, the epitaxial VO_2 thin film exhibits dramatic resistivity change by 4 orders of magnitude during its IMT by applying voltage bias, which is as large as that of the bulk VO_2[6]. The high quality epitaxial VO_2 thin film was employed to fabricate the simple single-pole single-throw (SPST) type switches. DC

characteristics of the VO_2 RF switches were measured and RF switching performances of switches by heating and applying voltage bias were compared. Also, measured electrical IMT by continuous square wave voltage bias and characterized electrical switching speed of the VO_2 RF switches were shown.

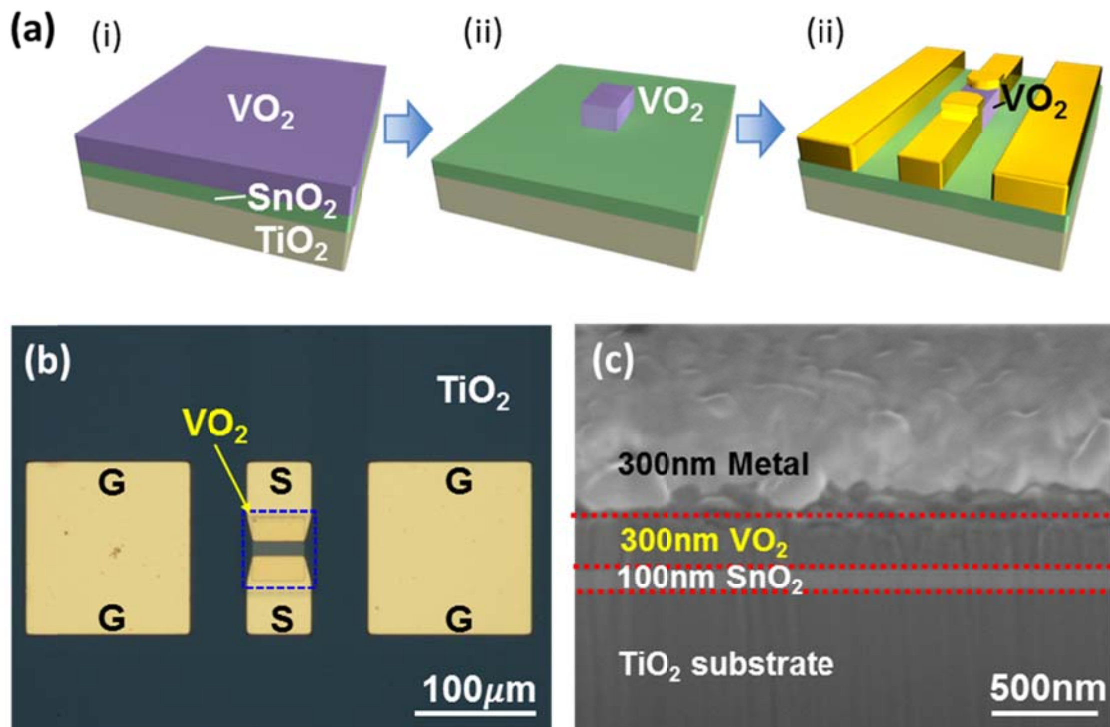

Figure 4.2 (a) A schematic illustration of the fabrication process for electrically triggered VO_2 RF switches. **(b)** A microscopic image. **(c)** A cross-sectional scanning electron microscope (SEM) image taken from the finished device.

Fig. 4.2 (a) shows the schematic illustration of the fabrication process. The VO_2 layer and the SnO_2 buffer layer were epitaxially grown on TiO_2 (001) substrate by pulsed laser deposition (Fig 4.2 (a) i), followed by patterning of the VO_2 layer using photolithography and reactive ion

etching (RIE) (Fig 4.2 (a) ii). Finally, microwave coplanar waveguide (CPW) lines were defined by photolithography and e-beam evaporation (Ti/Au, 10 nm/300 nm) (Fig 4.2 (a) iii). A microscopic image of the finished device is shown in Fig. 4.2 (b). The device structure and CPW design were simulated and optimized using Keysight ADS 2013 momentum. The length of the entire device was 140 µm. The width of the signal line and the ground line were 54 µm and 133 µm, with 43 µm spacing between signal and ground line. Input and output signal lines are separated with 10 µm spacing on the VO_2 layer. In Fig. 4.2 (c), a cross-sectional scanning electron microscope (SEM) image shows 100 nm SnO_2 buffer and 300 nm VO_2 layers.

4.3. DC characterization

After the device fabrication, the DC electrical characteristics were measured using HP 4155 semiconductor parameter analyzer in ambient air.

Fig. 4.3 (a) shows Current-Voltage (I-V) characteristic of electrically triggered IMT VO_2 devices. The electrical characteristic was obtained by double sweeping DC voltage bias to the device in series with various series resistors (R_s) from 1 kΩ to 6 kΩ to prevent damage from excessive current. Damage to the VO_2 layer was observed for the measurement with series resistor value smaller than 1 kΩ. Initially, the VO_2 layer under low voltage bias has a high resistance and it is in insulator phase which resulted in very low current. However, when the voltage reached the threshold value for IMT phase transition (V_{IMT}), the VO_2 became metallic and current was dramatically increased, which corresponds to the path (1) in Fig. 4.3 (a). It is worth noting that current level was increased, as the value of the series resistor was decreased, because total resistance across the device was decreased. Consequently, the V_{IMT} was reduced from 15.7 V to

13.1 V, as the series resistance value was decreased from 6 kΩ to 1.5 kΩ. When decreasing the voltage bias which corresponds to the path (2) in Fig. 4.3 (a), ~9V of hysteresis voltage gap was observed. The voltages for metal to insulator phase transition (V_{MIT}) were also varied from 7.2 V with a 6 kΩ series resistor to 3.9 V with a 1.5 kΩ series resistor.

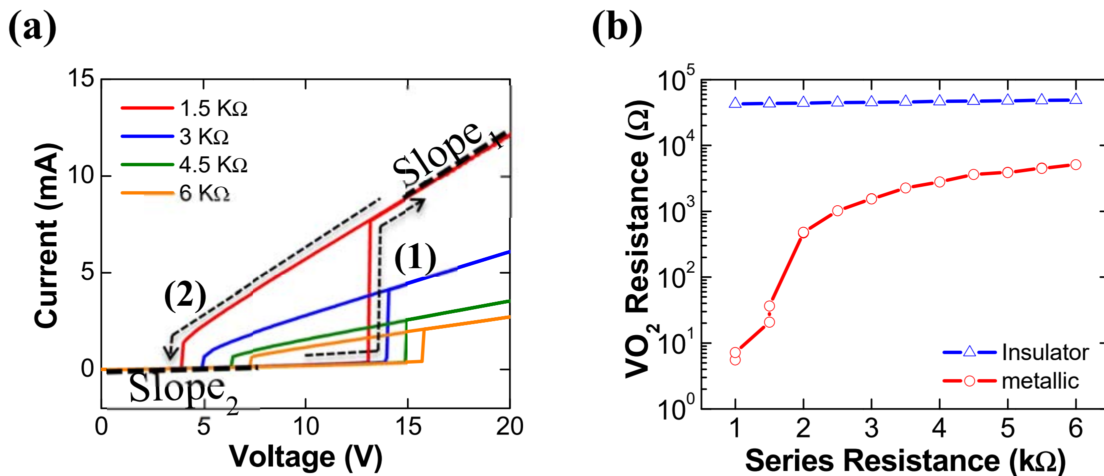

Figure 4.3 DC characteristics of the VO_2 RF switches. **(a)** I-V characteristic of VO_2 switches in series with 1.5 to 6 kΩ resistors. **(b)** The VO_2 resistance as a function of series resistance extracted from slopes of I-V curves in Fig. 4.3 (a).

Resistance of the VO_2 layer at the insulating phase and the metallic phase were carefully extracted from the slope of each the I-V curve with different series resistance values. For example, resistances of the VO_2 layer with 1.5 kΩ series resistor at the metallic phase and the insulating phase are displayed as a $slope_1$ and a $slope_2$, respectively in Fig. 4.3 (a). Then, as shown in Fig. 4.3 (b), the final resistance values of the VO_2 layer as a function of different series resistance values were calculated by the following formula: $R_{VO2} = (dV/dI) - R_S$. Interestingly, it

is found that the resistance of the VO_2 layer at the metallic state was significantly increased with the larger series resistor, while the VO_2 resistance remained the same at the insulating state. Such trend is largely attributed to the incomplete phase transition of the VO_2 layer under small current flow and electric field. When the voltage bias is applied to the VO_2, carriers are injected and this forms a narrow local metallic path in the VO_2. As time passes, the metallic area expands and eventually the entire layer goes through the phase transition. Thus, large series resistors suppress current level and result in partial phase transition in VO_2.

The VO_2 resistance with 1 kΩ series resistor was 5.5 Ω and 4.3 kΩ, at the metallic and the insulator phase respectively. Nearly 4 orders of magnitude change in resistance is comparable to device made of single crystalline bulk VO_2[6]. While other report shows the resistance change by electrical excitation is approximately one order of magnitude smaller than that of thermal excitation[61], The large resistivity change by electrical excitation in this work is also comparable to that of thermal excitation. This confirms that the electrical phase transition is as complete as thermal one.

4.4. RF characterization

The switching performance of the VO_2 RF switches were measured by scattering (S-) parameters under the frequency range from 45 MHz to 40 GHz using Agilent E8364A performance network analyzer (PNA). The VO_2 RF switches were tested and compared for both thermal and electrical trigger. A temperature controlled stage was used for thermally triggered VO_2 RF switches measurement. In order to make the VO_2 to be in fully metallic phase, the sample temperature was increased to 363 K, which is above the phase transition temperature ~341 K of VO_2[3]. To measure

electrically triggered VO_2 RF switches, 15 V DC bias was applied to the VO_2 RF switches in series with 1 kΩ resistor via bias T using HP E3631A power supply. Also, the VO_2 RF switches were simulated with Keysight ADS 2013 momentum.

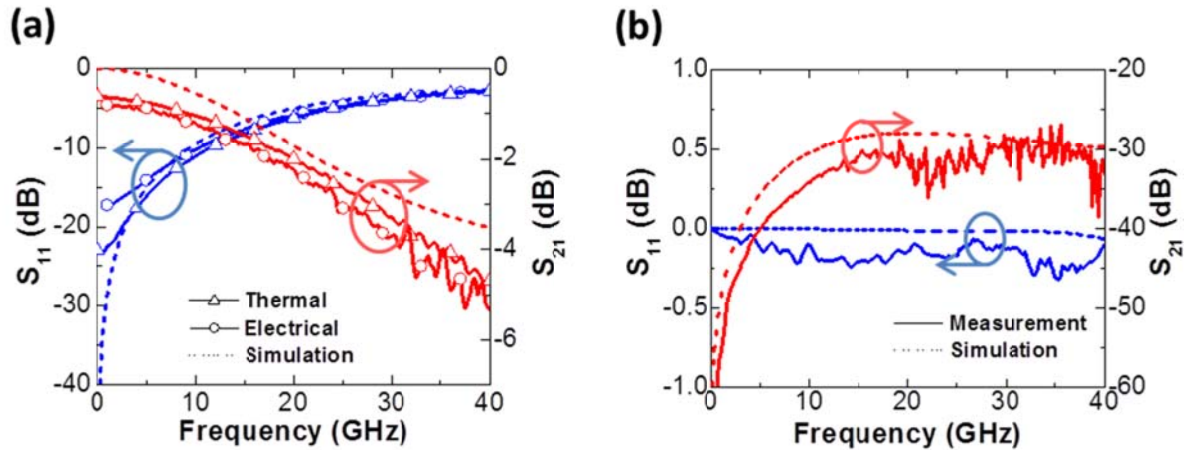

Figure 4.4 The measured and simulated S_{11} and S_{21} parameters of VO_2 RF switches in the frequency range from 45 MHz to 40 GHz **(a)** at the ON-state, and **(b)** at the OFF-state under a frequency range of 45 MHz to 40 GHz.

Measured and simulated RF characteristic of the VO_2 RF switches at the ON- and OFF- states are shown in Fig. 4.4. The result clearly indicates that the VO_2 RF switches became the ON-state when voltage bias was applied beyond V_{IMT} across the VO_2 layer or sample was heated above transition temperature (T_{IMT}). Once the phase transition to the metallic state occurs, the microwave single can be transmitted through the VO_2 CPW which becomes conductive. Fig. 4.4 (a) shows the RF characteristic of VO_2 RF switches at the ON-state. The insertion loss (S_{21}) of -3 dB was measured at 24.3 GHz and 27.7 GHz for electrically and thermally activated RF switches,

respectively, which confirms good phase transition of the VO_2 layer by both methods. The return losses (S_{11}) of VO_2 RF switches were measured to -4.7 dB at 24.3 GHz and -4.3 dB at 27.7 for electrically and thermally activated RF switches, respectively. The VO_2 RF switches became the OFF-state when switches were at below T_{IMT} or without voltage bias. Fig 4.4 (b) shows the RF characteristic of VO_2 RF switches at the OFF-state. S_{21} characteristics at the OFF-state showed low insertion loss of -25 dB over the entire frequency range. The simulated RF characteristics at the OFF-state agreed well with measured RF characteristics.

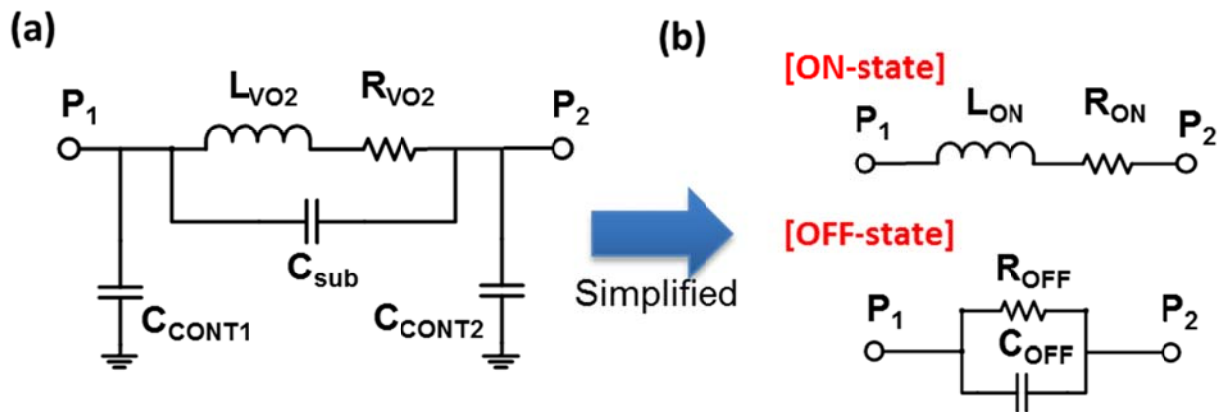

Figure 4.5 (a) An equivalent circuit model that was used to model VO_2 RF switches. **(b)** A simplified equivalent circuit model for the switch operation. The device is simplified to the RL series circuit at the ON-state and the RC parallel circuit at the OFF-state.

To further analyze RF switching characteristics, the two-port equivalent circuit model of the VO_2 RF switches were employed as shown in Fig. 4.5 (a)[57-59]. The parameters of each component inthe equivalent circuit were extracted from measured s-parameter from 45 MHz to 40 GHz. In the equivalent circuit model, C_{sub} modeled the parasitic capacitance of the VO_2 signal line, R_{VO2}

and L_{VO2} are the intrinsic resistance and reactance of the VO_2 layer, and C_{CONT1} and C_{CONT2} are parasitic capacitance between metal pads and the SnO_2/TiO_2 substrate. The parameters of each component at both ON- and OFF- states are shown in Table 4.1. Simplified equivalent circuits are illustrated in Fig. 4.5 (b). As the resistance of the VO_2 changes during the phase transition, two different simplified equivalent circuits are models for ON- and OFF-state. When the VO_2 RF switches operated at the OFF-state, it behaved as a parallel RC circuit with the resistance of 46 kΩ which blocked RF signals efficiently trough the CPW line. On the other hand, at the ON-state, the resistance of the device reduced to 4.6 Ω which is similar to a series RL circuit. The calculated resistance difference between the ON-state and the OFF-state is about 4 orders of magnitude, which well agrees to the measured resistance in Fig. 4.3 (b). The intrinsic cut-off frequency (F_{co}) is the one of the key value to decide the highest operation frequency and can be calculated by the following equation, $F_{CO}=1/(2\cdot\pi R_{on}\cdot C_{off})$, where R_{on} and C_{off} are the resistance at the ON-state and the capacitance at the OFF-state, respectively[60]. The VO_2 RF switches exhibit R_{on} of 4.6 Ω and C_{off} of 1.99 fF, resulting in F_{co} of 17.4 THz which is higher than previously reported RF switches based on polycrystalline VO_2[29, 30].

Components	**On (Metallic)**	**Off (Insulator)**
L_{VO2}(pH)	555	-
R_{VO2} (Ω)	4.6	4.6×10^4
C_{SUB}(fF)	-	2.7
C_{CONT1} (fF)	15	15
C_{CONT2} (fF)	15	15

Table 4.1 A comparison of extracted device model parameters for electrically triggered VO_2 RF switches at the ON- and OFF- states.

4.5. IMT switching speed characterization

One of the clear advantages of an electrical triggering method is that the transition can be completed much faster than other triggering methods, such as by heating or by shining light. In order to calculate actual phase transition time, the dynamic response measurements under different frequencies were performed by configuring the circuit as shown in Fig. 4.6 (a). Continuous square wave voltage under various frequencies from 10 kHz to 400 kHz was applied using the function generator (Tektronix FG5010) to the VO_2 RF switch in series with a 1.5 kΩ resistor. A voltage drop on the entire circuit (V_T), and a voltage drop only by the VO_2 (V_{VO2}) were monitored by the digital oscilloscope (Tektronix TDS2014B). The dynamic response of the VO_2 RF switches is shown in Fig. 4.6 (b).

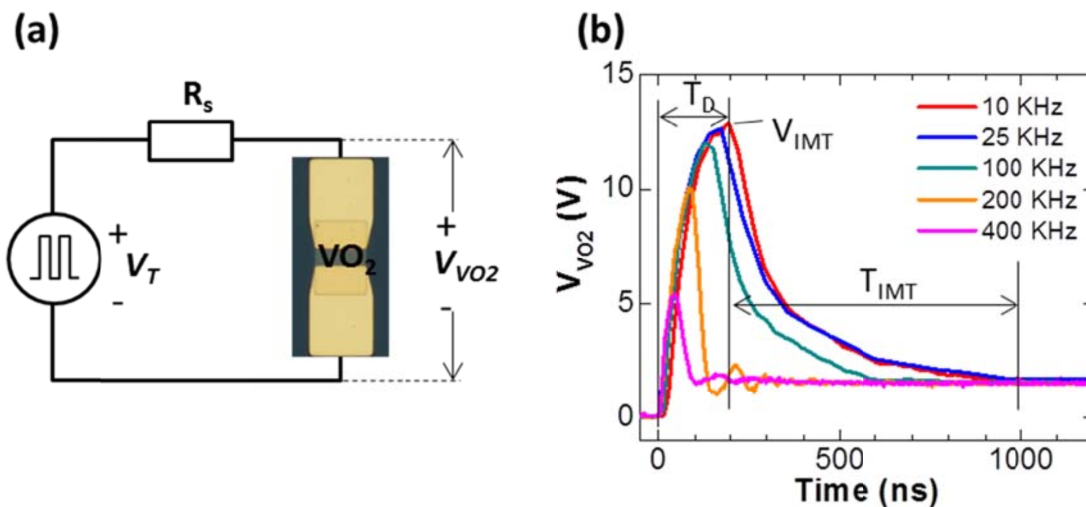

Figure 4.6 (a) A circuit schematic used to measure phase transition time. **(b)** Voltage response of the VO_2 RF switch with 1 kΩ series resistor under various frequencies from 10 kHz to 400 kHz.

When the VO_2 switch was at the insulator state (i.e., before reaching a V_{IMT}), resistance of the VO_2 switch is much larger than the resistance of the series resistor, thus most of the voltage drop is across VO_2 Switch. As applied voltage reached a V_{IMT}, VO_2 switch became metallic and the resistance of the VO_2 switch was abruptly decreased. Consequently, the voltage drop across the VO_2 switch was also decreased. Time required for electrical phase transition is the combination of two types of times, delay time (T_D) and actual insulator-to-metal transition time (T_{IMT})[62, 63]. T_D indicates the time required for the voltage drop on the VO_2 layer to reach a V_{IMT}. T_D can be further reduced by employing sharper voltage waveform and smaller series resistor. T_{IMT} is the duration of the phase transition. During this time, the VO_2 layer was exhibited sharp resistance drop. T_{IMT} can be expressed as $T_{IMT} = \tau_0 + RC$, where τ_0 is intrinsic rise time and RC is the RC time delay. As V_{VO2} reaches the V_{IMT} value, the filamentary low resistance current path is formed between electrodes[64]. Over the time, the current path expands by the current injection and joule heating so that the phase transition of the entire of the VO_2 layer is completed[65]. T_D and T_{IMT} for VO_2 RF switches with 1 kΩ series resistor are ~ 180 ns and ~840 ns, respectively. As the input frequency was increased, both V_{IMT} and T_{IMT} were decreased. Also, as the frequency is increased, intervals between voltage pulses are also decreased so that latent heat from the joule heating is not completely dissipated. Such estimation also indicates that the switching speed is largely dependent on T_{MIT} value.

Considering that the electrical phase transition occurs by current injection followed by joule heating, a theoretical minimum switching time, t_{min}, for the electrical phase transition can be calculated by using a simple thermal model[29, 30] with the following equation (2),

$$t_{min} = \frac{\rho_{VO2} * C_{VO2*}\text{volume} * \Delta T}{I * V} \quad (2)$$

Where ρ_{VO2} is the density of VO_2 (4340 kg m^{-3}), C_{VO2} is the heat capacity of VO_2 (690 J kg^{-1} K^{-1}), volume is the dimension of VO_2 (54 μm * 10 μm * 300 nm), ΔT is the temperature change of the film (341 K – 298 K = 43 K), V and I are voltage and current at the phase transition (13.1 V and 7.7 mA, from Fig. 4.3 (a)). The calculated t_{min} is 206 ns, which is approximately 4 times smaller than the measured result. Considering that joule heating is not the only factor that affects the phase transition and the actual device temperature is increased above the phase transition temperature, the calculated result is acceptable. Since both V_{IMT} and T_{MIT} are highly depends on the dimension of the VO_2, switching speed can be further enhanced by engineering the geometry of the device.

4.6. Summary

In this chapter, it is demonstrated that electrically triggered RF switches based on the epitaxially grown VO_2 thin film with the simple device structure. The high quality epitaxial VO_2 thin film was achieved by using the SnO_2 template layer in between the VO_2 layer and TiO_2 substrate, which enables to perform 4 orders of magnitude of resistance change by the electrical triggering. The VO_2 RF switches exhibit the S_{21} difference greater than 25 dB at 24 GHz by the electrical triggering, which implies that electrical IMT is comparable to other IMT approaches. The VO_2 RF switches also showed high frequency responses of insertion losses of -3 dB at the ON-state and return losses of -4.3 dB at the OFF-state over 24 GHz. The study on electrical IMT dynamics revealed 840 ns of phase transition time. The Epitaxial VO_2-based RF Switches demonstrate

good high frequency response and fast transition time, showing good potential for simply processed high frequency RF switches.

5. Silicon nanomembrane transferred optical switches on epitaxial VO_2

In the previous chapters, electrical properties of highly epitaxial VO_2 on SnO_2/TiO_2 were studied and thermally/electrically triggered RF switches were demonstrated. In this chapter, electrically triggered Si-VO_2 integrated optical switches are demonstrated, which utilize another novel property of VO_2 film, large optical constants change with the phase transition. This device consists of single crystalline Si nanomembrane (NM) and highly epitaxial VO_2 film on SnO_2/TiO_2. Nanomembrane transfer printing method enabled to integrate the Si NM and the VO_2 film. Thus, the optical switch can take advantage of both the single crystalline Si as an optical waveguide core and the VO_2 film as a switching material.

15V bias is used to induce the phase transition in the VO_2 and the switch exhibits extinction ratio (ER) of 15.05 dB and 13.83 dB and insertion loss (IL) of 2.48 dB and 3.41 dB by simulations and measurements, respectively. Measured turn on and turn off time was ~150 ns and ~250 ns, respectively.

5.1. Previous optical application devices based on VO_2

The VO_2 exhibits large optical constants change with phase transition and this made it attractive material for optical application devices. Refractive index, *n*, indicates the phase velocity of light in the medium, while extinction coefficient, *k*, indicates light attenuation. With utilizing and

engineering these properties, application devices can be designed such as optical modulators[15], optical switches[66], and optical resonators[67]. Hysteresis during the phase transition can be also applicable for optically controlled memory devices[68].

Newly developed highly epitaxial VO_2 thin film on SnO_2/TiO_2 structure can be an excellent candidate material for optical switches for a couple of reasons. First, large optical constant change can modulate optical signal propagation properties. Second, robust phase transition without cracking is suitable for repeated uses. Third, sharp phase transition and narrow hysteresis are required for fast switching speed.

5.2. Optical switching device design

Although the VO_2 shows large optical constant change with phase transition, there is limitation for directly using it as an optical medium to guide light because the VO_2 has relatively high extinction coefficient, k, for both insulator and metallic state. Thus, light transmitted through the VO_2 experiences large propagation loss. To circumvent this problem, integrated Si-VO_2 optical devices are proposed[15, 17]. Si-VO_2 integrated devices use conventional Si photonics device structure with depositing polycrystalline VO_2 on a small area. By employing this structure, mature silicon technology can be used and minimize the propagation loss from VO_2, but still utilizing novel properties of VO_2. However, this approach cannot be used for application devices using highly epitaxial VO_2 on SnO_2/TiO_2 substrate. In this work, instead, Si NM is transfer printed on top of VO_2 to fabricate Si- VO_2 integrated optical switches.

For the optical switches to be efficient, high extinction ratio is favorable while insertion loss needs to be suppressed. To satisfy these conditions, when the switches are at the ON-state, light

needs to be highly confined inside the Si waveguide with minimum interaction to lossy VO_2 layer. On the other hand, at the OFF-state, light needs to be less confined in the Si waveguide and absorbed by the VO_2 layer so that output is efficiently decreased.

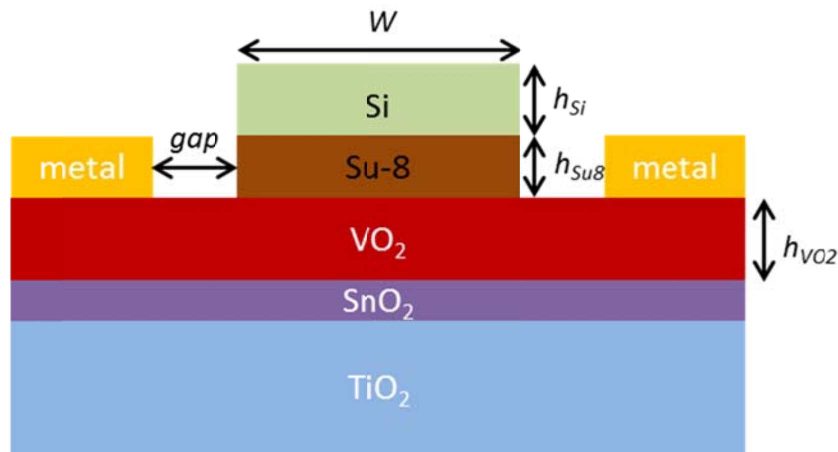

Figure 5.1 The schematic illustration of the cross section for Si- VO_2 integrated optical switches. Design parameters for optimized geometry are shown such as Si waveguide thickness h_{Si}, Si waveguide width w, VO_2 layer thickness h_{VO2}, Su-8 layer thickness h_{Su8}, and spacing between metal comtact and waveguide *gap*.

Optimized geometry of the devices within the fabrication capability is modeled by optical mode simulation (Lumerical mode sulutons). In fig. 5.1, design parameters to optimize the single mode optical switch are illustrated. Optimized waveguide structure has Si thickness, h_{si} = 190 nm, width w = 700 nm, and VO_2 thickness, h_{VO2} = 200 nm. While standard silicon-on-insulator (SOI) based single mode waveguide has thickness of 220 nm[69], thickness in this device was carefully chosen to be 190 nm to enhance the light interaction with the VO_2 layer below the waveguide. The other parameters are chosen considering the same reason. As the parameters are reduced too

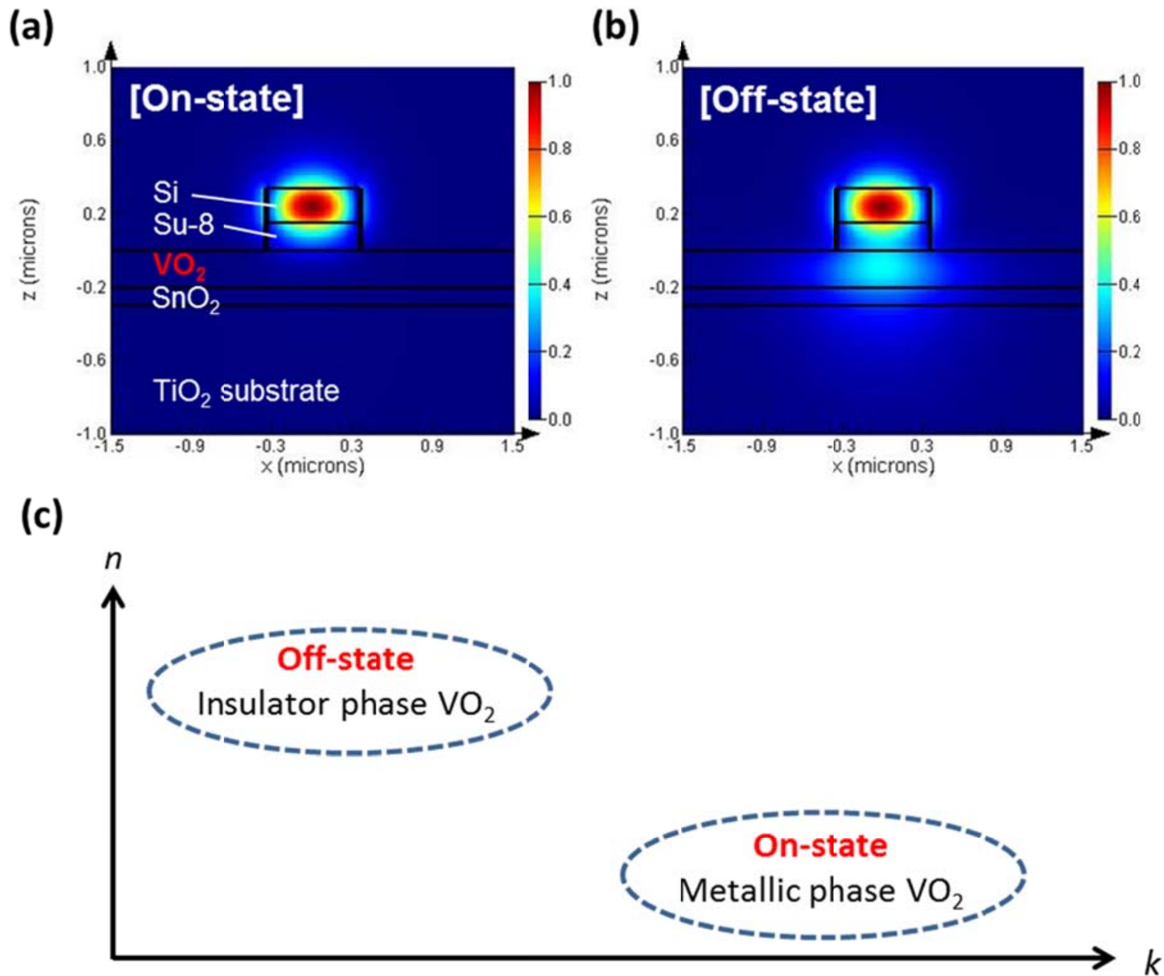

Figure 5.2 The Si- VO_2 integrated optical switch design. **(a), (b)** Simulated electric field profile when the VO_2 is in insulator phase and metallic phase, respectively. **(c)** A diagram shows relation between the operation of the optical switch and the optical constants of the VO_2.

much, the interaction between the optical mode and the VO_2 layer is increased too much, which results in high insertion loss. Su-8 layer is placed between the Si waveguide not only because it promotes adhesion of transfer printed Si NM but also it works as a cladding layer. Since refractive index of the Su-8 is approximately 1.5[70], high index contrast between Si waveguide core and Su-8 allows to efficiently confine the optical mode within the Si waveguide core.

Spacing between waveguide and metal pads, *gap*, does not affect much on optical mode because lateral optical confinement is good enough and light is well confined in the waveguide. However, smaller gap will improve switching speed.

Fig. 5.2 (a) and (b) show cross sectional electric filed profiles for the fundamental TE mode light in the optical switches. Fig. 5.2 (a) shows the ON-state profile and the optical mode is well confined in the Si waveguide core, which works as a single mode waveguide. The simulated effective index $n_{eff} = 2.48$ and the propagation loss is 0.24 dB/μm. Fig. 5.2 (b) shows the OFF-state and it is clearly seen that the optical mode interacts with lossy VO_2 layer. The effective index $n_{eff} = 2.51$ and the propagation loss is 2.0 dB/μm.

Interestingly, extinction coefficient of the VO_2 at the OFF-state is higher than that at the ON-state. As shown in fig. 5.2 (c), refractive index of the VO_2 at the metallic state is low, which leads to high index contrast with the Si core layer. Although the the VO layer absorbs more light at the metallic state, propagation loss at this state is smaller.

5.3. Device fabrication

Si-VO_2 integrated optical switch was constructed on VO_2 layer with transfer printed Si NM. The fabrication process starts with preparing Si NM. As shown in Fig. 5.3 (a), Si NM was prepared with silicon-on-insulator substrate (SOI, Soitec) with 205-nm-thick Si layer and 400-nm-thick buried oxide (BOX) SiO_2 layer. To make desired Si thickness of 190 nm, top Si layer on SOI was thinned down using thermal oxidation followed by wet etching of oxidation layer in HF. Etching holes are patterned on Si layer by photolithography and reactive ion etching in SF_6/O_2.

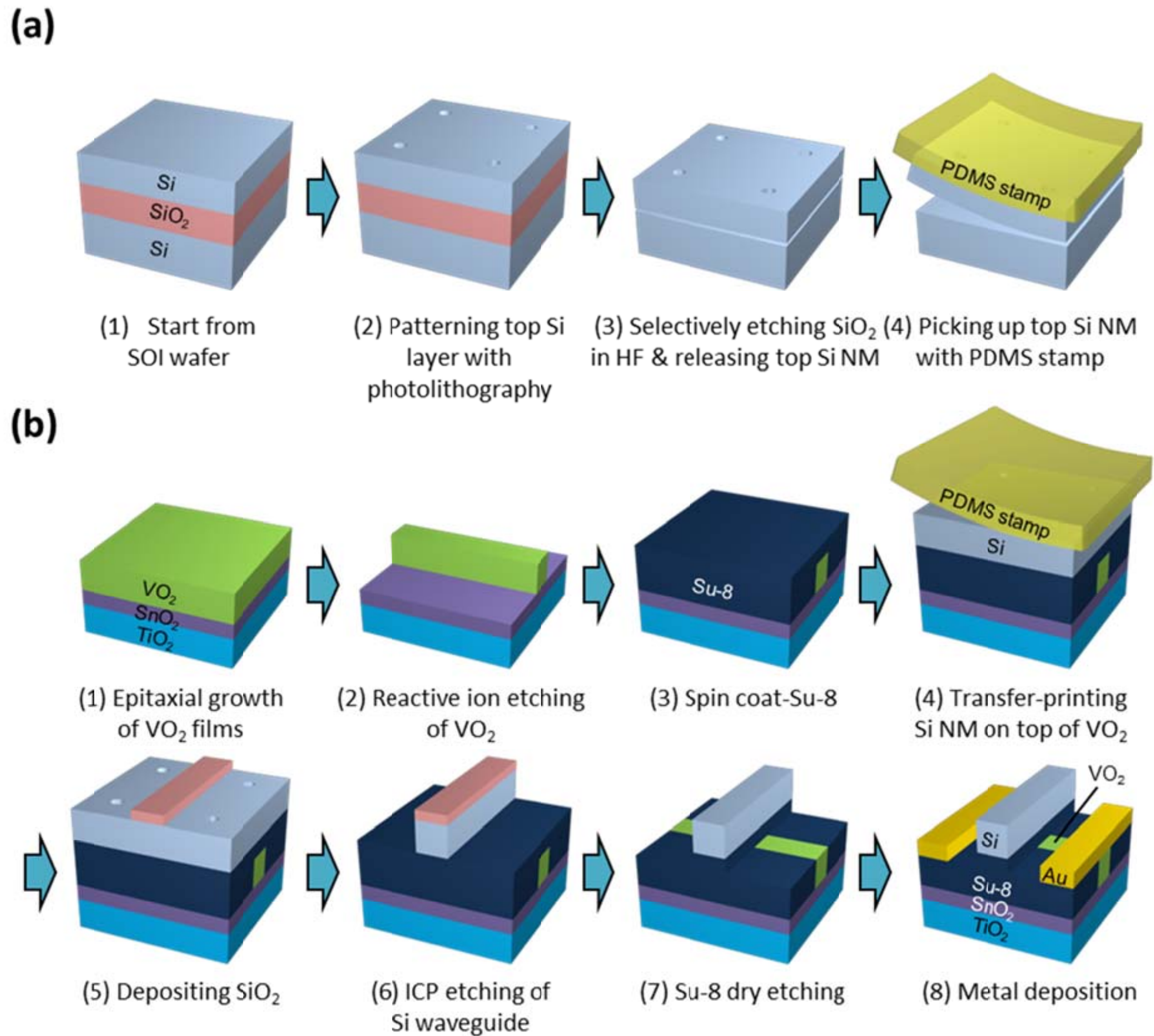

Figure 5.3 The fabrication process illustration. **(a)** Process illustration for preparing Si nanomembrane (NM). **(b)** Process illustration for fabricating an optical switch using Si NM and VO_2 on SnO_2/TiO_2.

In Fig. 5.3 (b), fabrication steps with prepared Si NM are illustrated. Si-VO_2 film was patterned by photolithography and reactive ion etching (RIE) in the CF_4 gas. Then, Si NM transfer onto VO_2 was performed by an elastomeric polydimethylsiloxane (PDMS) stamp transfer printing method[71, 72]. During the transfer, adhesive layer (Su-8 2000.5, Microchem Corp.) is spin-coated

on VO_2. Since the adhesive layer also serves as an optical cladding layer, thickness was adjusted to ~150 nm to maximize optical switching performance. After the transfer print, Si waveguide is defined by e-beam lithography and inductively coupled plasma (ICP) etching in Cl_2. Exposed adhesive Su-8 layer is also etched by RIE in O_2. Finally, metal electrodes of 10-nm-thick Ti and 300-nm-thick Au were formed by additional e-beam lithography, e-beam evaporation and lift off.

5.4. Device characterization

The phase transition in VO_2 is accompanied with a large change in optical constants. By utilizing this, the light confinement and transmission through Si waveguide can be electrically controlled. In Fig. 5.4 (a) and (b), ON- and OFF-state operation of the Si-VO_2 integrated optical switch is illustrated. Fig. 5.4 (c) and (d) show captured electric field intensity of fundamental TE mode continuous wave transmission through the Si waveguide by finite difference time domain (FDTD) simulation. When VO_2 is insulating (i.e., with n_{VO2} = 3.1), the light cannot be well propagating through Si waveguide with n_{Si} = 3.4, due to weak light confinement in Si core and light absorption in VO_2 with k = 0.3 (Fig. 5. 4 (a), (c)). On the other hand, when VO_2 is electrically switched to the metallic state (i.e., with n_{VO2} = 1.7), the mode becomes tightly confined inside the Si waveguide such that the transmission loss substantially decreases (Fig.5.4 (b), (d)), even though the k increases to around 3. While electron transport in electrical measurement could be triggered just by a local metallic path in VO_2, this optical transmission is determined by the overall fraction of metallized VO_2, and thus can give effective way to estimate the genuine switching speed of VO_2 by electric field.

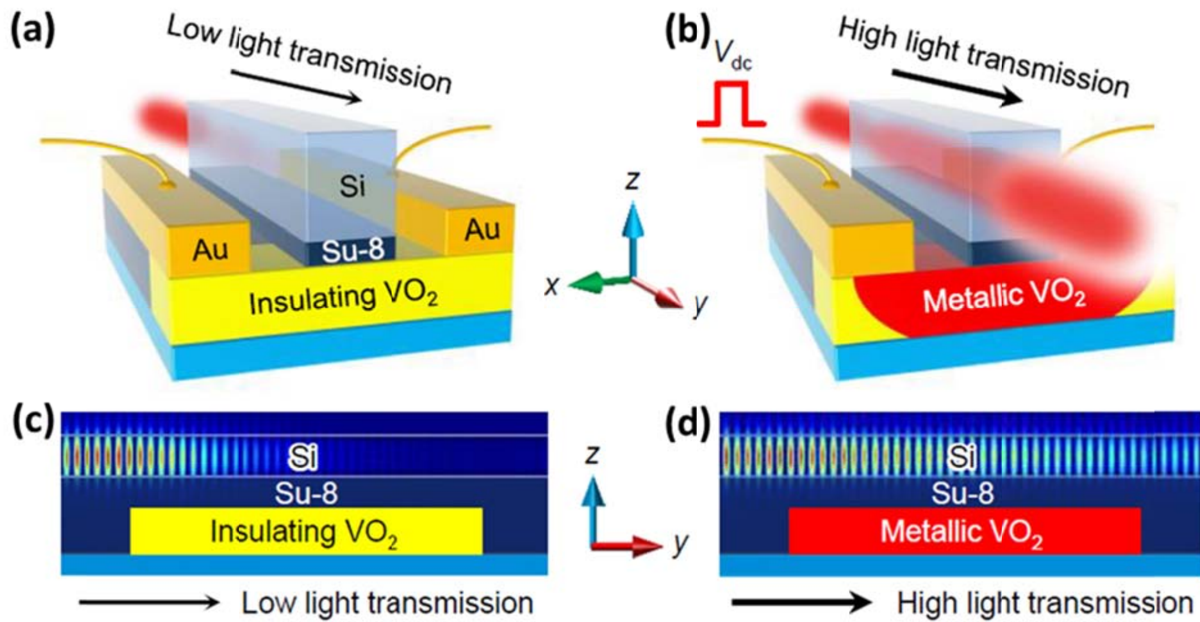

Figure 5.4 Electrically triggered optical switch using epitaxial VO_2. **(a), (b)** Schematic drawings for the optical modulator consisting of single crystalline Si waveguide and epitaxial VO_2 film (a) without and (b) with applying an external voltage V_{dc}. **(c), (d)** Simulated TE mode light propagation through the Si waveguide for the light wavelength λ of 1.55 µm, when the VO_2 is in the (c) insulating and (d) metallic states. The VO_2 layer can be metallized by applying V_{dc}, which is higher than a threshold voltage for IMT

To characterize the Si-VO_2 integrated optical switch, tunable laser (Tunics Plus) was used as a light source, optical spectrometer (Ocean Optics NIR-512) was used to measure optical transmission spectrum, and optical oscilloscope (Agilent 86116A) was used to measure optical switching performance. The laser was coupled into Si waveguide with single mode lensed fibers. Wide wavelength range of the input signal (1.5 µm to 1.6 µm with 0.25-µm step) is used to demonstrate wide bandwidth of the optical switch. The output optical signal from the Si waveguide was also coupled to single mode lensed fiber and sent to the spectrometer or the oscilloscope.

For transmission spectrum measurement, 15V DC voltage bias was applied to Au electrode by DC power supply (Agilent E3631a) and the output was monitored by the spectrometer. As shown in Fig. 5.5 (a), when external DC voltage, V_{dc}, was applied, the VO_2 layer became metallic and the switch turned on. Fig. 5.5 (b) compares FDTD simulation and measured for the extinction ratio and the insertion loss. At the wavelength of 1550 nm, the extinction ratio of 15.05 dB and 13.83 dB and the insertion loss of 2.48 dB and 3.41 dB were observed for the simulation and measurement, respectively.

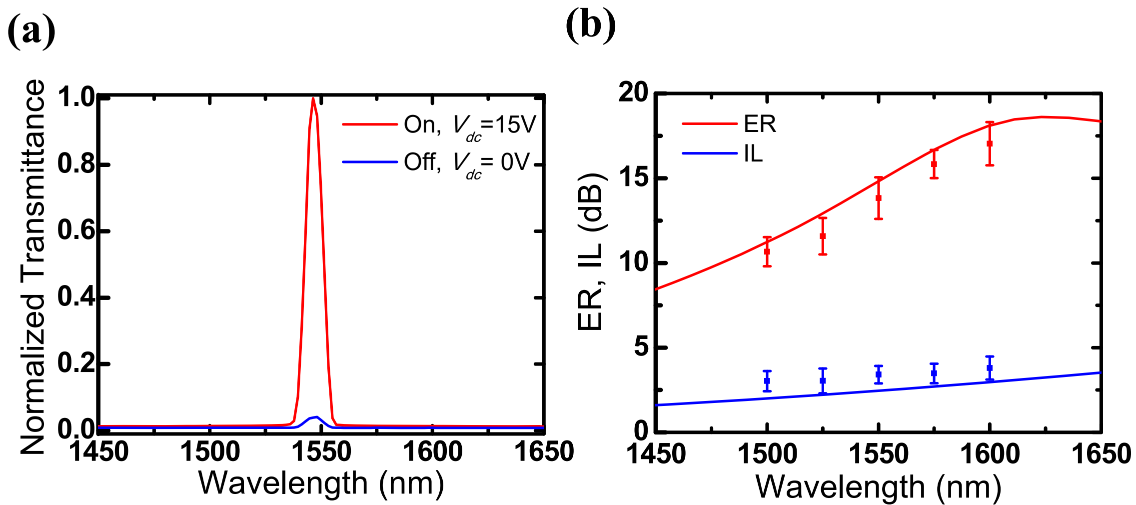

Figure 5.5 Electrically triggered light transmission in Si-VO_2 integrated optical switches. **(a)** Light transmission for the off (i.e., V_{dc} = 0 V) and on (i.e., V_{dc} = 15 V) state for a fixed wavelength λ of 1,550 nm. **(b)** The extinction ratio (ER) and the insertion loss (IL) of transmission as a function of λ. Squares with error bars and black solid line correspond to the experimental and simulated results, respectively.

For the switching speed the measurement, 15-V peak to peak (in the range of 0 V to 15 V) square wave in 1-MHz frequency was applied to Au electrode by function generator (Tektronix FG5010)

and the output was monitored by the oscilloscope. A 1 kΩ resistor was connected in series to the optical switch to suppress the current level and avoid burning the device.

When the electric field is applied to VO_2 drives carrier injection, which induces formation of a local metallic path in VO_2 on a short time scale of <1 ns[73]. However, after the local metallic path formation, the electric field falls and a thermal process by Joule heating follows with the relation, $\Delta T \propto 1 - \exp(-t/\tau)$, where τ is a time constant. When the electric field is removed, the reverse metal-to-insulator transition is also governed by a cooling process with $\Delta T \propto \exp(-t/\tau)$. These indicate that the switching speed in VO_2 could generally be limited to thermal processes. Thus, the sharp phase transition with a narrow hysteresis in $VO_2/SnO_2/TiO_2$ film would naturally allow a fast switching by electric field.

Fig. 5.6 (a) and (b) show the time-dependent optical transmission upon the application and removal of electric field for VO_2/TiO_2- and $VO_2/SnO_2/TiO_2$-based optical swithes. The light transmission became 10~100-times enhanced upon the application of electric field, consistent with our device simulations. Regarding the switching speed, the $VO_2/SnO_2/TiO_2$-based device exhibited the full transition of light transmission on time scales of ~150 ns and ~250 ns during the on and off switchings, respectively, which were 3~4 times shorter than those of VO_2/TiO_2-based device. By fitting, the time constant τ is estimated be ~36 ns and ~74 ns during the on and off switching, respectively, for $VO_2/SnO_2/TiO_2$-based device, whereas they were ~91 ns and ~252 ns during the on and off switching, respectively, for VO_2/TiO_2-based device. The switching speed became much enhanced possibly due to the sharp phase transition of the newly developed SnO_2-templated films, but it could be further improved later by optimizing the device design.

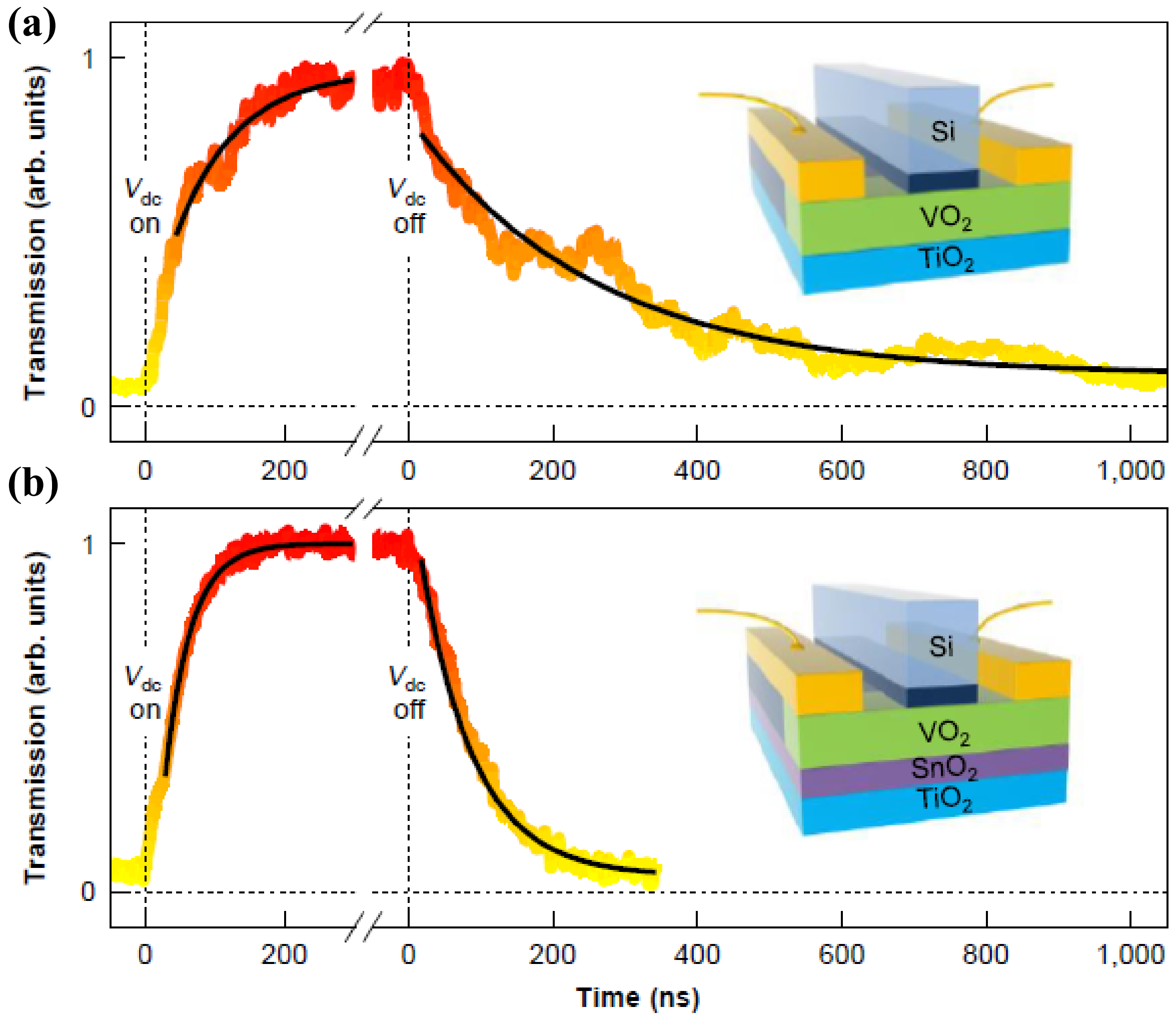

Figure 5.6 Measured optical transmission as a function of time t for λ = 1.55 μm, when V_{dc} is switched on and off for **(a)** VO_2/TiO_2- and **(b)** $VO_2/SnO_2/TiO_2$-based devices. The magnitude of transmission is also expressed in color from yellow (low transmission) to red (high transmission). Black solid lines are the fitted results with the formula of $1 - \exp(-t/\tau)$ and $\exp(-t/\tau)$.

5.5. Summary

In this chapter, Si-VO_2 integrated optical switches were demonstrated to avoid large optical propagation loss from the VO_2. The device design to take advantage of large optical constant

changes in VO_2 was explored. The designed switch is ON-state with metallic phase VO_2 and OFF-state with insulator VO_2. The switch can be turned on by applying 15 V DC bias with extinction ratio of 13.83 dB and insertion loss of 3.41 dB for the wavelength of 1550 nm, which well agrees with FDTD simulations. The switching speed of the device was also monitored. The sharp phase transition by highly epitaxial VO_2 on SnO_2/TiO_2 results in fast switching speed. The switch showed turn on and off time of ~ 150 ns and ~ 250 ns, respectively.

6. Conclusion

This dissertation shows dedicated work on the development of a novel correlated oxide material and their device applications. The VO_2 that was focused in this thesis has received attention for decades due to its attractive properties. The VO_2 undergoes an insulator-to-metal phase transition slightly above room temperature. In single crystalline bulk VO_2, a sharp electrical resistivity change and optical constant change are observed during the phase transition. The transition is also accompanied with a monoclinic to rutile structural phase transition. However, there have been challenges to find a way to grow single crystalline high quality thin film VO_2, which limits developing high performance application devices. Thus, polycrystalline VO_2 has been used for devices but they often suffer from degraded properties such as cracks in the thin film, phase transition temperature shifts, reduced resistivity change ratio, and reliability issues. A new structure of epitaxial VO_2 was presented in this work by SnO_2 template engineering. The VO_2 on SnO_2/TiO_2 exhibit properties as good as single crystalline bulk VO_2. With utilizing such properties, the epitaxial VO_2 based electrical RF switches and optical switches were developed and their characteristics were demonstrated.

Measured electrical and optical properties of the epitaxial VO_2 were discussed in chapter 2. The resistivity change in epitaxial VO_2 films was monitored under vacuum as temperature increased. The measurement showed the resistivity change of 4 orders of magnitude during the IMT, which is comparable to that of single crystalline bulk VO_2. Additionally, the phase transition width, ΔT, was as small as ~0.8 K and the hysteresis loop gap was as narrow as ~ 5 K, which confirms the high quality of the epitaxial VO_2 films. The changes in optical constants were measured by

ellipsometry for the wavelength range of 900 nm to 1650 nm and the temperature range of 298 K to 353 K. Abrupt changes in optical constants were observed near 340 K. Refractive index change, Δn, was ~1.4 and extinction coefficient change, Δk, was ~2.7.

In chapter 3, the demonstration of thermally triggered RF switches based on epitaxial VO_2 thin film with the simple device structure was presented. Fast IMT at a low temperature allowed VO_2 RF switches to exhibit sharp resistivity changes with the S_{21} change greater than 15 dB at 333 K and 339 K for IMT and MIT, respectively. VO_2 RF switches performed the sharp transition of S_{21} less than 3 K and showed a low loss operation frequency up to 24.2 GHz with a low insertion loss of -1.36 dB and isolation of 17.56 dB at 12.03 GHz.

Chapter 4 showed electrically triggered RF switches based on the epitaxial VO_2 thin film with the simple device structure. The turn-on voltage of 13.1 V and resistivity change of 4 orders of magnitude was observed for electrical IMT. The VO_2 RF switches exhibit the S_{21} difference greater than 25 dB at 24 GHz by the electrical triggering, which implies that electrical IMT is comparable to other IMT approaches. The VO_2 RF switches also showed high frequency responses of insertion losses of -3 dB at the ON-state and return losses of -4.3 dB at the OFF-state over 24 GHz. The study on electrical IMT dynamics revealed 840 ns of phase transition time. The switching speed of the RF switches was also investigated. Theoretical switching speed during IMT was calculated to ~206 ns, while the measured value was ~840 ns. The Epitaxial VO_2-based RF Switches demonstrate good high frequency response and fast transition time, showing good potential for simply processed RF switches.

In chapter 5, Si-VO_2 integrated optical switches were demonstrated. Since the optical properties of VO_2 were not suitable for optical waveguide core, Si waveguide was integrated to avoid large optical propagation loss from the VO_2. Thus, the device that can take advantage of large optical

constant changes in VO_2 was designed. The designed switch exhibits ON-state with metallic phase VO_2 and OFF-state with insulator phase. When 15 V DC bias was applied, the extinction ratio of 13.83 dB and insertion loss of 3.41 dB for the wavelength of 1550 nm were observed, which well agrees with FDTD simulations. The switching speed of the device was also monitored. The sharp phase transition by highly epitaxial VO_2 on SnO_2/TiO_2 results in fast switching speed. The switch showed turn on and off time of ~ 150 ns and ~ 250 ns, respectively.

Appendix

A.Optical constants of VO_2

To measure optical constants of VO_2, 300nm of highly epitaxial VO_2 was grown on TiO_2 substrate with 100 nm SnO_2 template layer. Spectroscopic ellipsometry (J.A. Woollam M-2000 ellipsometer) and temperature controlled stage (Bioscience tools temperature controller) were used for the measurement. The refractive index *n* and extinction coefficient *k* were obtained by changing beam angle from 60 to 75 degree with 5 degree step for the wavelength range of 900 nm to 1650 nm. To see the optical constant change as a function of temperature, the stage temperature is changed from 298 K to 353 K. The scan repeated for every 1 degree with 0.1 K resolutions. The optical constants for SnO_2 and TiO_2 were separately measured and taken into consideration for obtaining optical constants of VO_2 using Cauchy modelling.

A.1. Optical constants vs. temperature

Table A.1 shows that the refractive index change, Δn of ~1.36 and ~1.54 and the extinction coefficient change, Δk of ~2.67 and 1.96 for the wavelength of 1550 nm and 1310 nm, respectively.

Temperature, K	Refractive index, *n*		Extinction coefficient, *k*	
	1310 nm	1550 nm	1310 nm	1550 nm
298	3.0706	3.1057	0.40925	0.29949
299	3.0706	3.1057	0.40925	0.29949
300	3.0706	3.1057	0.40925	0.29949

301	3.07085	3.10555	0.410365	0.300815
302	3.0711	3.1054	0.41148	0.30214
303	3.07075	3.1051	0.412465	0.302695
304	3.0704	3.1048	0.41345	0.30325
305	3.0717	3.1071	0.414025	0.30403
306	3.073	3.1094	0.4146	0.30481
307	3.07005	3.10385	0.41394	0.304835
308	3.0671	3.0983	0.41328	0.30486
309	3.066	3.11125	0.414235	0.309705
310	3.0649	3.1242	0.41519	0.31455
311	3.0674	3.1182	0.41592	0.31289
312	3.0699	3.1122	0.41665	0.31123
313	3.0699	3.1151	0.418145	0.312275
314	3.0699	3.118	0.41964	0.31332
315	3.06805	3.1228	0.419895	0.315525
316	3.0662	3.1276	0.42015	0.31773
317	3.0675	3.11925	0.42072	0.31631
318	3.0688	3.1109	0.42129	0.31489
319	3.0657	3.1126	0.422145	0.31464
320	3.0626	3.1143	0.423	0.31439
321	3.06475	3.11675	0.424935	0.317585
322	3.0669	3.1192	0.42687	0.32078
323	3.06675	3.1128	0.42715	0.321595
324	3.0666	3.1064	0.42743	0.32241
325	3.06535	3.10515	0.42905	0.327735
326	3.0641	3.1039	0.43067	0.33306
327	3.0614	3.1033	0.43393	0.33217
328	3.0573	3.1044	0.43496	0.33707
329	3.0497	3.0991	0.44198	0.3457
330	3.0432	3.0836	0.44986	0.35536
331	3.0337	3.0908	0.45642	0.36766
332	3.0195	3.0807	0.46659	0.38248
333	3.0022	3.063	0.48282	0.40732
334	2.9806	3.0425	0.50985	0.44135
335	2.9728	3.0329	0.54122	0.48391
336	2.9446	3.0311	0.58061	0.54095
337	2.8769	2.9671	0.7018	0.67576
338	2.8052	2.9355	0.8572	0.86531
339	2.6925	2.8792	1.102	1.1753
340	2.5425	2.7632	1.407	1.5339
341	2.3318	2.596	1.7011	1.9272
342	2.1378	2.4248	1.9229	2.2359
343	2	2.2828	2.0552	2.4155

344	1.8642	2.1527	2.1528	2.6131
345	1.7198	1.9766	2.2565	2.7656
346	1.6482	1.8931	2.2986	2.8675
347	1.6008	1.8443	2.3263	2.8873
348	1.5731	1.8056	2.349	2.9331
349	1.5552	1.7737	2.3632	2.9497
350	1.5414	1.7701	2.3729	2.9654
351	1.53895	1.76085	2.3672	2.96835
352	1.5365	1.7516	2.3615	2.9713
353	1.5276	1.74985	2.3674	2.96655
354	1.5187	1.7481	2.3733	2.9618
355	1.52325	1.75055	2.3813	2.9693
356	1.5278	1.753	2.3893	2.9768
357	1.5239	1.748	2.38245	2.9918
358	1.52	1.743	2.3756	3.0068
359	1.515	1.7415	2.37615	2.99665
360	1.51	1.74	2.3767	2.9865
361	1.5171	1.74075	2.3792	2.9948
362	1.5242	1.7415	2.3817	3.0031
363	1.5244	1.7433	2.38025	2.9901
364	1.5246	1.7451	2.3788	2.9771
365	1.52455	1.73955	2.3807	2.97465
366	1.5245	1.734	2.3826	2.9722
367	1.52035	1.73725	2.3712	2.96275
368	1.5162	1.7405	2.3598	2.9533
369	1.5215	1.7481	2.36795	2.96915
370	1.5268	1.7557	2.3761	2.985
371	1.5253	1.7556	2.37645	2.98025
372	1.5238	1.7555	2.3768	2.9755
373	1.5294	1.742	2.3681	2.9704

Table A.1. The refractive index *n* and extinction coefficient *k* as a function of temperature at the fixed telecommunication wavelengths of 1310 nm and 1550 nm

A.2. Optical constants vs. wavelength

Table A.2 shows that the refractive index and the extinction coefficient as a function of wavelength.

Wavelength, nm	Refractive index, *n*		Extinction coefficient, *k*	
	298 K	373 K	298 K	373 K
1101.4	2.976772	1.450608	0.497708	1.754648
1104.8	2.981158	1.4499	0.496304	1.76085
1108.2	2.983619	1.458196	0.49594	1.784155
1111.6	2.9829	1.451528	0.494635	1.785962
1115.1	2.9867	1.448728	0.493849	1.796646
1118.5	2.987031	1.45178	0.492232	1.804504
1121.9	2.99042	1.453847	0.491701	1.818385
1125.3	2.990742	1.455386	0.490024	1.832396
1128.8	2.990474	1.452867	0.489533	1.843874
1132.2	2.996201	1.451565	0.488089	1.850649
1135.6	2.99682	1.457232	0.486273	1.866128
1139	2.998834	1.449965	0.485356	1.876128
1142.5	3.000148	1.459278	0.484632	1.887853
1145.9	3.003395	1.456611	0.483368	1.895511
1149.3	3.005457	1.454947	0.482008	1.91041
1152.7	3.005638	1.453155	0.480631	1.910452
1156.2	3.007107	1.457834	0.479586	1.932109
1159.6	3.01093	1.454389	0.477927	1.939268
1163	3.012789	1.454789	0.477134	1.948814
1166.4	3.015534	1.455459	0.475693	1.960546
1169.9	3.013318	1.460104	0.474439	1.973455
1173.3	3.017714	1.457231	0.472561	1.978483
1176.7	3.018229	1.457601	0.471379	1.992959
1180.1	3.021859	1.453135	0.469728	1.995216
1183.6	3.024187	1.461682	0.468736	2.014743
1187	3.023976	1.464492	0.46685	2.021721
1190.4	3.024809	1.459097	0.465925	2.039727
1193.8	3.02743	1.464926	0.464092	2.037341
1197.3	3.027357	1.466656	0.462468	2.054066

1200.7	3.031558	1.467255	0.460864	2.058828
1204.1	3.032245	1.47333	0.459468	2.080145
1207.6	3.03297	1.466709	0.45784	2.084244
1211	3.035709	1.46401	0.456852	2.092082
1214.4	3.036676	1.469019	0.455264	2.099747
1217.8	3.039889	1.471457	0.453979	2.107673
1221.3	3.037461	1.473013	0.451279	2.12105
1224.7	3.040064	1.476368	0.45046	2.138523
1228.1	3.042853	1.47821	0.448395	2.13859
1231.5	3.043758	1.475073	0.447464	2.153626
1235	3.044174	1.483614	0.445842	2.16697
1238.4	3.04511	1.487201	0.443554	2.178315
1241.8	3.049246	1.482407	0.442474	2.185156
1245.2	3.046162	1.484498	0.441485	2.186122
1248.7	3.052375	1.484876	0.439033	2.203256
1252.1	3.051893	1.492855	0.438192	2.220519
1255.5	3.051168	1.490917	0.435035	2.237308
1258.9	3.055701	1.495272	0.435199	2.230806
1262.4	3.055511	1.498014	0.432511	2.247741
1265.8	3.059234	1.497678	0.431652	2.250951
1269.2	3.05518	1.508297	0.429086	2.265413
1272.7	3.059583	1.502989	0.428494	2.272111
1276.1	3.061915	1.502791	0.426118	2.277734
1279.5	3.059725	1.504983	0.424289	2.294859
1282.9	3.063641	1.504519	0.423408	2.29366
1286.4	3.065209	1.512953	0.422085	2.313212
1289.8	3.064922	1.515328	0.418769	2.325429
1293.2	3.065523	1.513908	0.418032	2.31592
1296.6	3.06553	1.513968	0.416048	2.339982
1300.1	3.065373	1.524779	0.414999	2.360215
1303.5	3.069325	1.518874	0.412467	2.355764
1306.9	3.068527	1.529315	0.411493	2.36978
1310.3	3.070593	1.529416	0.409252	2.368067
1313.8	3.070354	1.518852	0.40787	2.388499
1317.2	3.076891	1.522517	0.40753	2.381307
1320.6	3.07369	1.536326	0.405102	2.400778
1324.1	3.07425	1.537748	0.402944	2.418886
1327.5	3.076143	1.534564	0.401478	2.413848
1330.9	3.071696	1.540136	0.398575	2.424
1334.3	3.07748	1.540737	0.398416	2.455049
1337.8	3.081437	1.542575	0.397029	2.446619
1341.2	3.080713	1.550008	0.396064	2.464319
1344.6	3.080562	1.555447	0.392881	2.459744

1348	3.08293	1.552113	0.391292	2.475861
1351.5	3.082463	1.554634	0.389239	2.475894
1354.9	3.081374	1.553271	0.388314	2.499774
1358.3	3.084871	1.565957	0.386006	2.520649
1361.8	3.082989	1.564694	0.385038	2.51684
1365.2	3.083744	1.567553	0.383112	2.509067
1368.6	3.084536	1.560653	0.381481	2.51918
1372	3.084117	1.584103	0.379629	2.545658
1375.5	3.086062	1.573557	0.378293	2.529863
1378.9	3.087637	1.580521	0.375839	2.545868
1382.3	3.088573	1.596909	0.374791	2.563141
1385.8	3.08637	1.58216	0.37374	2.563168
1389.2	3.086816	1.592311	0.371939	2.583959
1392.6	3.08862	1.599952	0.370227	2.573433
1396	3.091348	1.60494	0.367664	2.629159
1399.5	3.087469	1.598921	0.365915	2.603208
1402.9	3.094012	1.606577	0.36626	2.615195
1406.3	3.088824	1.598409	0.362751	2.628518
1409.8	3.091116	1.601064	0.361478	2.630308
1413.2	3.090351	1.618107	0.360682	2.656705
1416.6	3.092085	1.614441	0.358055	2.641301
1420	3.095153	1.60763	0.35615	2.638721
1423.5	3.093601	1.622715	0.356619	2.678592
1426.9	3.094155	1.624222	0.352856	2.686189
1430.3	3.092429	1.641296	0.352772	2.680421
1433.8	3.097876	1.628469	0.35051	2.688057
1437.2	3.095472	1.61929	0.349176	2.695823
1440.6	3.094386	1.632597	0.346568	2.71904
1444	3.100421	1.62699	0.34643	2.705801
1447.5	3.096781	1.642158	0.343784	2.713549
1450.9	3.095667	1.655245	0.342085	2.757662
1454.3	3.097792	1.658435	0.340963	2.75123
1457.8	3.09752	1.641895	0.339785	2.740757
1461.2	3.100333	1.667917	0.338371	2.748428
1464.6	3.098771	1.656243	0.33647	2.768767
1468	3.098491	1.68358	0.335042	2.771691
1471.5	3.098165	1.676327	0.333012	2.77291
1474.9	3.097946	1.676755	0.331216	2.802906
1478.3	3.100403	1.668506	0.330073	2.790312
1481.8	3.105203	1.667155	0.330506	2.799837
1485.2	3.097506	1.681505	0.326689	2.824692
1488.6	3.103372	1.685499	0.326187	2.829278
1492.1	3.101621	1.671207	0.323898	2.819779

1495.5	3.105449	1.678959	0.323183	2.825051
1498.9	3.102038	1.708801	0.319597	2.855818
1502.3	3.104899	1.696126	0.320059	2.850373
1505.8	3.104883	1.692193	0.318417	2.864347
1509.2	3.106449	1.697701	0.318758	2.866004
1512.6	3.101599	1.708067	0.315336	2.875575
1516.1	3.102338	1.717357	0.315263	2.888228
1519.5	3.104899	1.711222	0.311457	2.901345
1522.9	3.103404	1.716499	0.309402	2.904956
1526.4	3.106957	1.70847	0.310341	2.907486
1529.8	3.101947	1.752391	0.306837	2.945636
1533.2	3.103415	1.720389	0.307288	2.914067
1536.7	3.098823	1.737176	0.304896	2.953512
1540.1	3.104393	1.733561	0.304822	2.950641
1543.5	3.106088	1.739304	0.302496	2.926986
1546.9	3.104479	1.742382	0.300221	2.982435
1550.4	3.105652	1.741967	0.299488	2.970417
1553.8	3.107046	1.738048	0.300845	2.9534
1557.2	3.107726	1.752223	0.297967	2.953802
1560.7	3.106026	1.759784	0.295664	2.994443
1564.1	3.104808	1.763362	0.292711	3.022554
1567.5	3.108548	1.756659	0.29382	2.992556
1571	3.105073	1.766537	0.288985	3.026283
1574.4	3.109477	1.759975	0.291401	3.000155
1577.8	3.106633	1.762399	0.288385	3.004632
1581.3	3.108063	1.778373	0.287419	3.0238
1584.7	3.111788	1.761777	0.287213	3.022668
1588.1	3.112136	1.746558	0.285916	3.012676
1591.6	3.106935	1.790075	0.27954	3.059512
1595	3.10242	1.792538	0.273171	3.068006
1598.4	3.104871	1.806844	0.27901	3.060294
1601.9	3.110625	1.795399	0.277236	3.055918
1605.3	3.095643	1.805339	0.267648	3.085782
1608.7	3.118871	1.815236	0.274739	3.110124
1612.2	3.103926	1.839283	0.270968	3.141401
1615.6	3.118758	1.795516	0.275118	3.084103
1619	3.100732	1.829884	0.26964	3.118664
1622.4	3.105702	1.844866	0.270022	3.147077
1625.9	3.091136	1.848914	0.258574	3.153085
1629.3	3.101633	1.841971	0.265008	3.175501
1632.7	3.100993	1.845108	0.259691	3.15199
1636.2	3.097902	1.84771	0.261773	3.150163
1639.6	3.097341	1.86796	0.254453	3.153906

1643	3.110161	1.803602	0.263094	3.098634
1646.5	3.106075	1.870347	0.254733	3.147334
1649.9	3.12185	1.831434	0.261026	3.133298

Table A.2. The refractive index *n* and extinction coefficient *k* as a function of wavelength at room temperature (298 K) and high temperature (373 K)

B. Fabrication process for Si- VO_2 integrated optical switches

B.1. Dry etching of VO_2

To fabricate VO_2 application devices including Si-VO_2 integrated optical switches, defining device area in VO_2 is essential so that patterning and etching techniques for VO_2 needs to be addressed. In this section, previous reports on VO_2 etching methods are briefly reviewed. Also, demonstration of ICP and RIE etching for device fabrication are presented.

Previous reports present that strong acid or base solutions can rapidly etch VO_2[74, 75]. Since too fast etching speed is undesirable for accurate process control, wet etching is not an ideal option for patterning VO_2. Several reports also present dry etching techniques. It was demonstrated that VO_2 can be etched by general gases available for reactive ion etching (RIE) such as CF_3, CF_4 and SF_6[74]. However, these fluoride based plasma etching have relatively high etch rate (> 100 nm / min.) and totally isotropic etching profile. Thus, these gases are not suitable for accurate etching depth control or vertical side wall etching profile. Other reports showed an inductively coupled plasma (ICP) etching with Cl_2 and Ar[76, 77]. By modifying Cl_2/Ar mixing ratio, the etch rate and anisotropic etching profile can be adjusted. Although this method has most desirable etching conditions, dielectric etching mask layer is required. Cl_2 gas is used to etch but it also etches most metals. Physical bombarding by Ar gas can damage photoresists. Thus, metal or photoresist etching mask is not suitable for deep ecth.

Fig. B.1 shows the scanning electron microscope (SEM) image for the etching profile of VO_2 by ICP with Cl_2/Ar. The image was taken with 70 degree tilted to clearly see the etching profile. On (100) TiO_2 substrate, 100nm SnO_2 and 300 nm VO_2 are epitaxially grown for the etching test. First, 200 nm SiO_2 etching mask area was defined by photolithography and electron beam evaporation of SiO_2 followed by lift-off. Dielectric mask was chosen since metal or photoresist mask cannot stand long etching time. The sample was etched for 4 min in a gas mixture of Cl_2 (10 sccm) and Ar (30 sccm) with the pressure of 5 mTorr, the RF power of 200 W, and the ICP power of 500 W. For this dry etching method, accurate etch depth control and smooth etched surface were achieved. 77 degree side wall angle was observed and a little roughness was projected to sidewall from the SiO_2 etching mask.

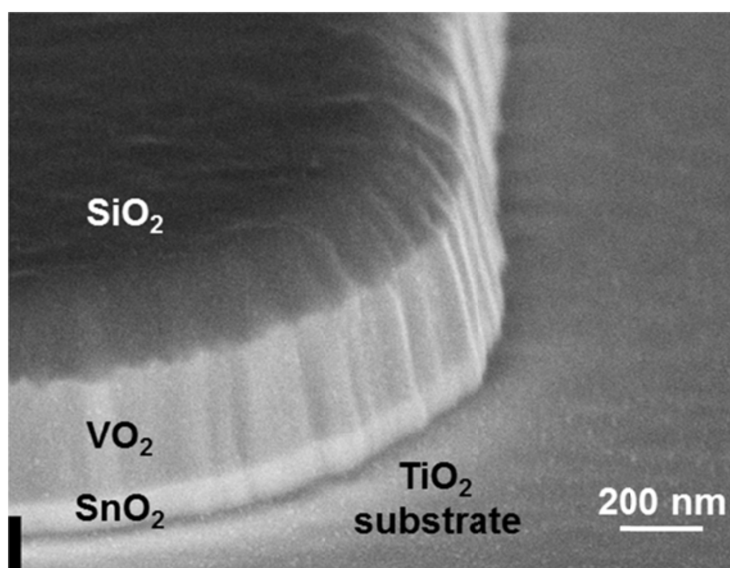

Figure B.1 70 degree tilted SEM image for the etching profile of VO_2on SnO_2/ TiO_2 by ICP with Cl_2/Ar.

For the Si-VO_2 integrated optical switches fabrication, RIE with CF_4 gas was employed because smooth etching profile was not critical for the device performance. 200 nm VO_2 on SnO_2/TiO_2 was prepared by pulsed laser deposition (PLD) and 10 μm long VO_2 according to the device design simulation. The sample was etched by photolithography with AZ 1813 photoresist. Subsequently it is etched by RIE in in a gas mixture of CF_4 (45 sccm) and O_2 (5 sccm) with the pressure of 40 mTorr and the power of 100 W. Fig. B.2 shows the optical microscopic image of the etched sample.

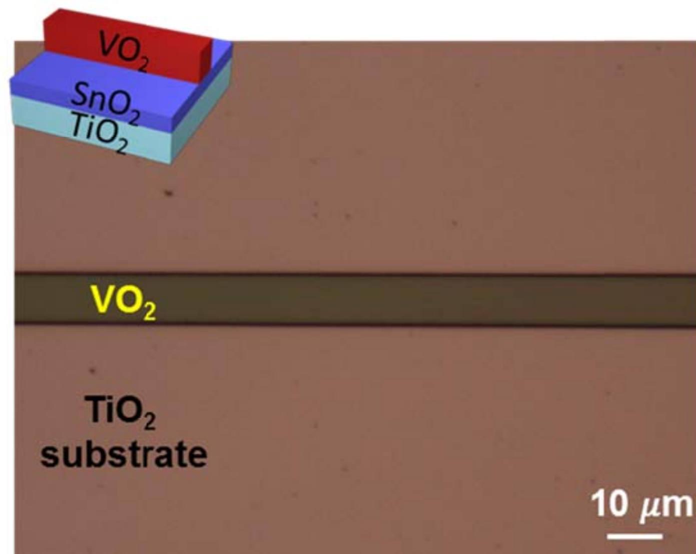

Figure B.2 Microscopic image of the etched VO_2 on SnO_2/ TiO_2 by RIE with CF_4. The inset illustration shows the 3D structure of the sample.

B.2. Si nanomembrane (NM) transfer printing

To achieve Si-VO_2 integrated optical switches, Si nanomembrane (NM) transfer printing method was employed. Although selectively etching nanomembranes from silicon-on-insulator (SOI) or

III-V material were introduced since decades ago[78, 79], nanomembranes have not received attention until transfer printing technique was introduced. Releasing and transfer printing NM to foreign substrates using elastomeric polydimethylsiloxane (PDMS) stamp opened a completely new paradigm of device fabrication[71, 72]. Thanks to this NM transfer printing method, optical switches benefited from both Si and VO_2 were realized.

B.2.1. Preparing silicon-on-insulator (SOI)

Detailed fabrication process starts with thinning down the top Si layer in SOI (SOITEC, 205 nm/400 nm, Si/Buried oxide) from 205 nm to 190 nm. As thermal oxidation of the SOI is conducted, the top Si layer is oxidized and silicon dioxide (SiO_2) growth occurs 54 % above and 46 % below the original surface of the SOI[80]. The thermal oxidation time is thickness was carefully calculated to achieve the desired thickness of the top Si. After and after the oxidation, the SOI was immersed in hydrogen fluoride (HF) solution to remove grown SiO_2 and thinned down, smooth top Si layer SOI was fabricated.

B.2.2. Releasing nanomembrane (NM)

Periodic small holes are patterned on the top Si layer in SOI by photolithography with AZ 1813 photoresist followed by RIE with SF_6/O_2. The holes in top SOI layer are essential to release relatively large size (> 100 * 100 μm^2) NM for selective wet etching of buried oxide (BOX) layer underneath the top Si. The size of etching holes and distance between holes should be kept small to ensure enough area in the top Si area, but they need to be large enough to have a reasonable selective etching time. In this work, the hole size of 5 μm and distance between holes of 50 μm were used.

The patterned SOI is then immersed in hydrogen fluoride (HF) solution to selectively etching BOX layer. The solution penetrates through patterned etch holes in the top Si layer and from the sides of SOI, and etches away the BOX layer. When the BOX layer is completely removed, the top Si layer falls down and sits on the bottom Si substrate. It should be noted that since the thickness of the BOX layer affects the etching time of it, appropriate thickness for the BOX layer need to be carefully chosen. Too thin BOX layer (< 200 nm) is difficult to be etched away since the path for the HF solution to penetrate through is too narrow. On the other hand, too thick (> 2000 nm) BOX is not preferred, either since the top Si layer may not directly fall down to the bottom Si substrate. SOI with BOX layer removed was taken out of the HF solution and gently cleaned the residual etching solution with deionized (DI) water. Since the bonding force between the top Si and the bottom Si is weak, the released top Si layer can be picked up by PDMS stamp.

B.2.3. Su-8 assisted transfer printing

To transfer print released Si NM, adhesion layer of Su-8 2000.5 (Microchem Corp.) is spin-coated on the destination substrate. Su-8 is a UV curable epoxy with cyclopentanone as a solvent, which not only promotes adhesion between the NM and the destination substrate but also works as an optical cladding layer to guide light for the Si-VO_2 integrated optical switches.

To achieve the desired device performance, the Su-8 coating thickness was adjusted by diluting the concentration of it with mixing additional solvent, cyclopentanone[81, 82]. Fig. B.3 shows the thickness change of diluted Su-8 2000.5 with cyclopentanone. A mixture of Su-8/cyclopentanone is spin-coated on Si with 5500 rpm and the thickness ware measured after baking the sample at 100 $^{\circ}$C for 10 min. The desired thickness of ~150 nm can be achieved by the Su-8 fraction of 0.6 in the mixture of Su-8/cyclopentanone.

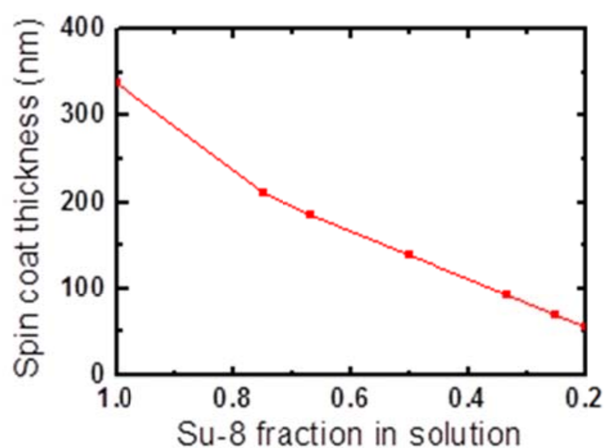

Figure B.3 Thickness change of diluted Su-8 2000.5 as a function of the fraction in a mixture of Su-8/ cyclopentanone. The su-8 mixture is spin-coated with 5500 rpm.

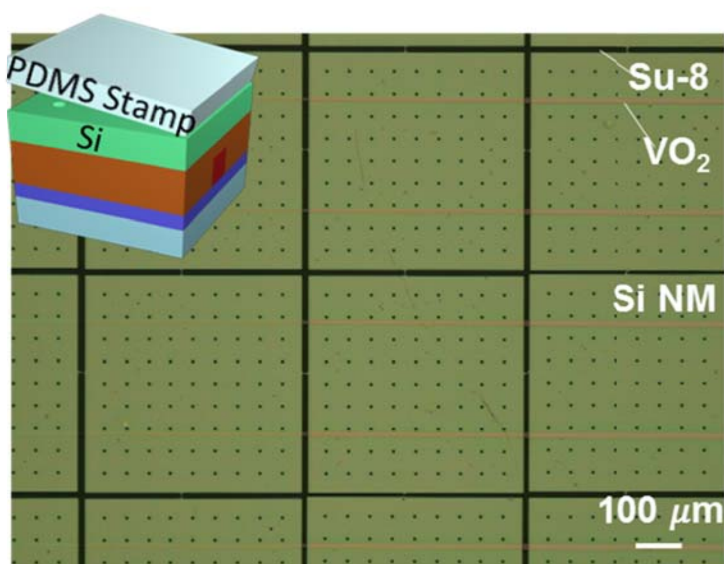

Figure B.4 Microscopic image of the Si NM transfer printed VO_2 on SnO_2/ TiO_2. The inset illustration shows the 3D structure of the sample.

The picked up Si NM with PDMS stamp is transfer printed on Su-8 coated VO_2. Then, the PDMS stamp was gently peeled off with Si NM adhered on the VO_2. Fig. B.4 shows the micro

scope image after the transfer printing is completed. To avoid cracks during the transfer printing of a large Si NM, an array of Si NMs (in size of 350*350 μm^2) were transfer printed. Since Si NM and Su-8 adhesion layers are very thin, the patterned VO_2 underneath the Su-8 is visible.

B.3. Optical waveguide patterning on Si

After transfer printing of Si NM on the VO_2, optical waveguide was patterned on the Si layer. Since side wall roughness is closely related to the propagation loss of the waveguide, smooth and vertical etching profile is critical[83].

This process requires the pattern resolution of 700 nm for the waveguide width and electron-beam (e-beam) lithography was employed as photolithography has limited pattern resolution. 950 PMMA C4 was spin-coated on the sample at 5000 rpm and baked for 3 min at 150 ^{o}C. Then, the sample was exposed with an e-beam using LEO 1530 system. The pattern was developed in MIBK:IPA 3:1 solution for 70 s. Subsequently, 200 nm SiO2 was deposited as an etching mask by electron beam evaporation followed by lift off. Fig. B.5 shows the microscopic image of deposited 700 nm wide SiO_2 etching mask on the Si NM. The SiO_2 etching mask was especially chosen since this endures longer during the following ICP etching than photoresist.

To pattern Si ridge waveguide, ICP etching in Cl_2/O_2 was employed to achieve anisotropic etching and smooth sidewall[84]. The sample was dry etched in ICP for 90 s in a gas mixture of Cl_2 (24 sccm) and O_2 (6 sccm) with the pressure of 10 mTorr, the RF power of 70 W, and the ICP power of 500 W. Also, the exposed Su-8 underneath the etching Si NM was etched by RIE O_2 plasma.

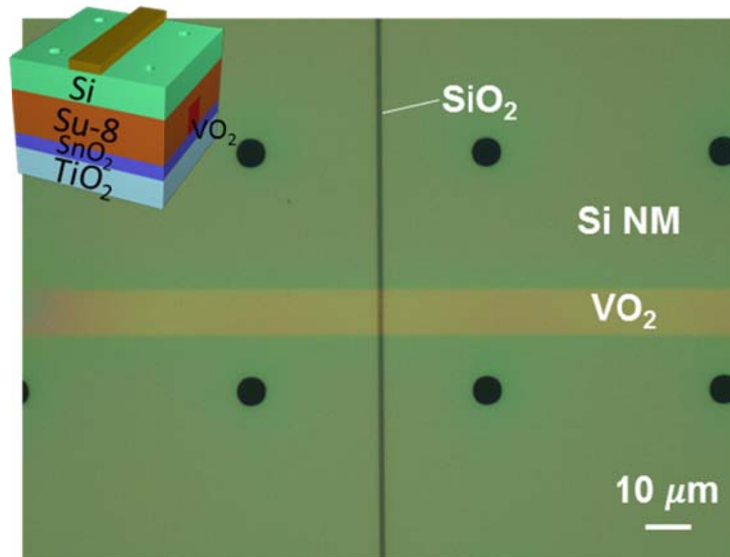

Figure B.5 Microscopic image of the 700 nm width SiO_2 etching mask on the Si NM. The inset illustration shows the 3D structure of the sample.

B.4. Metal electrode deposition

On the exposed VO_2 layer metal electrodes were deposited for the electrically triggered phase transition. As the distance between metal electrodes is reduced, the turn on voltage for electrical phase transition is decreased, which improves switching speed and reduces the power consumption. Thus, e-beam lithography was used to define metal electrodes.

Double coated PMMA was used to ensure thick resist coating for 300 nm metal electrodes deposition. 950 PMMA C4 was spin-coated on the sample at 5000 rpm and baked for 3 min at 150 ^{o}C and the same process repeated again to stack thick resist. Then, the sample was exposed with an e-beam using LEO 1530 system. With the careful alignment of the metal electrodes, they were placed with a ~2 μm spacing from the waveguide ridge. The pattern was developed in MIBK:IPA 3:1 solution for 70 s. Then, 10 nm/ 300 nm of Ti/Au metal stack was deposited by

electron beam evaporation followed by lift-off. Fig.B.6 shows the microscopic image of the device with metal electrodes deposited. It is clearly seen that 10 μm long VO_2 layer is placed underneath the Si waveguide with Su-8 cladding.

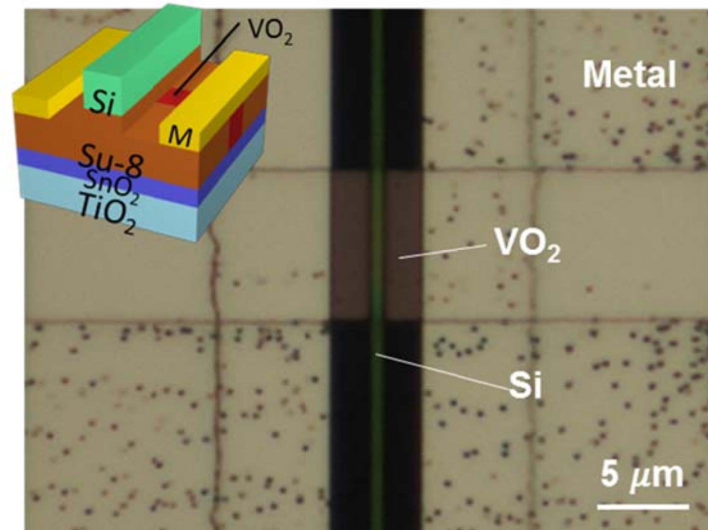

Figure B.6 Microscopic image of the Si-VO2 integrated optical switch. The distance between metal electrodes of 5 μm was defined by e-beam lithography. The inset illustration shows the 3D structure of the sample.

References

1. M.-K. Wu, J. R. Ashburn, C. J. Torng, P. H. Hor, R. L. Meng, L. Gao, Z. J. Huang, Y. Wang and a. Chu, Physical Review Letters **58** (9), 908 (1987).
2. Y. Tokura, Colossal Magnetoresistance Oxides (Gordon & Breach, 2000) (2000).
3. Z. Yang, C. Y. Ko and S. Ramanathan, Annu Rev Mater Res **41**, 337-367 (2011).
4. B. S. Mun, K. Chen, J. Yoon, C. Dejoie, N. Tamura, M. Kunz, Z. Liu, M. E. Grass, S.-K. Mo and C. Park, Physical Review B **84** (11), 113109 (2011).
5. C. Blaauw, F. Leenhouts, F. van der Woude and G. Sawatzky, Journal of Physics C: Solid State Physics **8** (4), 459 (1975).
6. D. Lee, J. Lee, K. Song, F. Xue, S.-Y. Choi, Y. Ma, J. Podkaminer, D. Liu, L.-Q. Chen, S. H. Oh, Z. Ma and C.-B. Eom, (unpubilshed) (2016).
7. M. F. Becker, A. B. Buckman, R. M. Walser, T. Lépine, P. Georges and A. Brun, Applied Physics Letters **65** (12), 1507-1509 (1994).
8. G. Stefanovich, A. Pergament and D. Stefanovich, Journal of Physics: Condensed Matter **12** (41), 8837 (2000).
9. J. Schutze, H. Ilgen and W. R. Fahrner, IEEE transactions on industrial electronics **48** (2), 281-285 (2001).
10. J. Darabi and K. Ekula, Microelectronics Journal **34** (11), 1067-1074 (2003).
11. Y. Joo, K. Dieu and C.-J. Kim, ASME-PUBLICATIONS-HTD **319**, 117-122 (1995).
12. H.-T. Kim, B.-G. Chae, D.-H. Youn, S.-L. Maeng, G. Kim, K.-Y. Kang and Y.-S. Lim, New Journal of Physics **6** (1), 52 (2004).
13. T. Driscoll, H.-T. Kim, B.-G. Chae, M. Di Ventra and D. Basov, Applied physics letters **95** (4), 043503 (2009).

14. T. Driscoll, H.-T. Kim, B.-G. Chae, B.-J. Kim, Y.-W. Lee, N. M. Jokerst, S. Palit, D. R. Smith, M. Di Ventra and D. N. Basov, Science **325** (5947), 1518-1521 (2009).

15. R. M. Briggs, I. M. Pryce and H. A. Atwater, Optics express **18** (11), 11192-11201 (2010).

16. J. D. Ryckman, V. Diez-Blanco, J. Nag, R. E. Marvel, B. Choi, R. F. Haglund and S. M. Weiss, Optics express **20** (12), 13215-13225 (2012).

17. A. Joushaghani, J. Jeong, S. Paradis, D. Alain, J. S. Aitchison and J. K. Poon, Optics express **23** (3), 3657-3668 (2015).

18. R. Scherwitzl, P. Zubko, I. G. Lezama, S. Ono, A. F. Morpurgo, G. Catalan and J. M. Triscone, Advanced materials **22** (48), 5517-5520 (2010).

19. P. Ruello, S. Zhang, P. Laffez, B. Perrin and V. Gusev, Physical Review B **79** (9), 094303 (2009).

20. J. Shi, Y. Zhou and S. Ramanathan, Nature communications **5** (2014).

21. F. Conchon, A. Boulle, R. Guinebretière, C. Girardot, S. Pignard, J. Kreisel, F. Weiss, E. Dooryhée and J.-L. Hodeau, Applied Physics Letters **91** (19), 192110-192110 (2007).

22. H. Liang, R. Soref, J. Mu, A. Majumdar, X. Li and W.-P. Huang, Journal of Lightwave Technology **33** (9), 1805-1813 (2015).

23. H. Lv, H. Wan and T. Tang, IEEE Electron Device Letters **31** (9), 978-980 (2010).

24. M. Imada, A. Fujimori and Y. Tokura, Reviews of Modern Physics **70** (4), 1039 (1998).

25. A. Zylbersztejn and N. F. Mott, Physical Review B **11** (11), 4383 (1975).

26. A. Barker Jr, H. Verleur and H. Guggenheim, Physical Review Letters **17** (26), 1286 (1966).

27. D. Maurer and A. Leue, Materials Science and Engineering: A **370** (1), 440-443 (2004).

28. N. B. Aetukuri, A. X. Gray, M. Drouard, M. Cossale, L. Gao, A. H. Reid, R. Kukreja, H. Ohldag, C. A. Jenkins and E. Arenholz, Nature Physics **9** (10), 661-666 (2013).

29. S. D. Ha, Y. Zhou, C. J. Fisher, S. Ramanathan and J. P. Treadway, Journal of Applied Physics **113** (18), 184501 (2013).

30. F. Dumas-Bouchiat, C. Champeaux, A. Catherinot, A. Crunteanu and P. Blondy, Applied Physics Letters **91** (22), 223505-223505 (2007).

31. M. Gurvitch, S. Luryi, A. Polyakov and A. Shabalov, Journal of Applied Physics **106** (10), 104504 (2009).

32. E. Abreu, M. Liu, J. Lu, K. G. West, S. Kittiwatanakul, W. Yin, S. A. Wolf and R. D. Averitt, New Journal of Physics **14** (8), 083026 (2012).

33. Z. Yang, C. Ko and S. Ramanathan, Journal of Applied Physics **108** (7), 073708 (2010).

34. H. T. Zhang, L. Zhang, D. Mukherjee, Y. X. Zheng, R. C. Haislmaier, N. Alem and R. Engel-Herbert, Nature communications **6**, 8475 (2015).

35. G. T. Reed, G. Mashanovich, F. Gardes and D. Thomson, Nature photonics **4** (8), 518-526 (2010).

36. P. Hindle, Microwave Journal **53** (11), 20-36 (2010).

37. S. Lucyszyn, IEE Proceedings-Science, Measurement and Technology **151** (2), 93-103 (2004).

38. G. M. Rebeiz and J. B. Muldavin, Microwave Magazine, IEEE **2** (4), 59-71 (2001).

39. J. Lampen, S. Majumder, R. Morrison, A. Chaudhry and J. Maciel, International Journal of RF and Microwave Computer-Aided Engineering **14** (4), 338-344 (2004).

40. C. L. Goldsmith, Z. Yao, S. Eshelman and D. Denniston, Microwave and Guided Wave Letters, IEEE **8** (8), 269-271 (1998).

41. D. Saias, P. Robert, S. Boret, C. Billard, G. Bouche, D. Belot and P. Ancey, Solid-State Circuits, IEEE Journal of **38** (12), 2318-2324 (2003).

42. P. Sun, P. Upadhyaya, D.-H. Jeong, D. Heo and G. S. La Rue, Microwave and Wireless Components Letters, IEEE **17** (5), 352-354 (2007).

43. J. Bellantoni, D. Bartle, D. Payne, G. McDermott, S. Bandla, R. Tayrani and L. Raffaelli, Microwave Theory and Techniques, IEEE Transactions on **37** (12), 2162-2165 (1989).

44. H. Ishida, Y. Hirose, T. Murata, Y. Ikeda, T. Matsuno, K. Inoue, Y. Uemoto, T. Tanaka, T. Egawa and D. Ueda, Electron Devices, IEEE Transactions on **52** (8), 1893-1899 (2005).

45. A. Koudymov, X. Hu, K. Simin, G. Simin, M. Ali, J. Yang and M. Asif Khan, Electron Device Letters, IEEE **23** (8), 449-451 (2002).

46. D. Gotch, Microwave Journal **50** (11), 24-36 (2007).

47. H. Lo, *Probe reconfigurable phase change material switches*. (ProQuest, 2009).

48. N. El-Hinnawy, P. Borodulin, B. P. Wagner, M. R. King, J. S. Mason, E. B. Jones, V. Veliadis, R. S. Howell, R. M. Young and M. J. Lee, presented at the Compound Semiconductor Integrated Circuit Symposium (CSICS), 2013 IEEE, 2013 (unpublished).

49. W. Wang, R. Zhao, L. Shi, X. Miao, P. Tan, M. Hong, T. Chong, Y. Wu and Y. Lin, Journal of applied physics **98** (12), 124313 (2005).

50. C.-Y. Wen, E. Chua, R. Zhao, T. Chong, J. Bain, T. Schlesinger, L. Pileggi and J. Paramesh, presented at the Electron Devices Meeting (IEDM), 2010 IEEE International, 2010 (unpublished).

51. K. Chen, L. Krusin-Elbaum, D. Newns, B. Elmegreen, R. Cheek, N. Rana, A. Young, S. Koester and C. Lam, IEEE Electron Device Letters **29** (1), 131-133 (2008).

52. N. El-Hinnawy, P. Borodulin, B. P. Wagner, M. R. King, E. B. Jones, R. S. Howell, M. J. Lee and R. M. Young, Applied Physics Letters **105** (1), 013501 (2014).

53. Y. Shim, G. Hummel and M. Rais-Zadeh, presented at the Micro Electro Mechanical Systems (MEMS), 2013 IEEE 26th International Conference on, 2013 (unpublished).

54. N. El-Hinnawy, P. Borodulin, E. B. Jones, B. P. Wagner, M. R. King and J. S. Mason, presented at the CS MANTECH Conf., May 19th-22nd, 2014 (unpublished).

55. J. Cho, L. Weiss, C. Richards, D. Bahr and R. Richards, Journal of Micromechanics and Microengineering **17** (9), S217 (2007).

56. Z. Yang, C. Ko, V. Balakrishnan, G. Gopalakrishnan and S. Ramanathan, Physical Review B **82** (20), 205101 (2010).

57. R. N. Simons and G. E. Ponchak, Microwave Theory and Techniques, IEEE Transactions on **36** (12), 1796-1803 (1988).

58. M. Naghed and I. Wolff, Microwave Theory and Techniques, IEEE Transactions on **38** (12), 1808-1815 (1990).

59. S. Gevorgian, P. L. Linner and E. L. Kollberg, IEEE Transactions on Microwave Theory Techniques **43**, 772-779 (1995).

60. M. Golio, *The RF and microwave handbook*. (CRC press, 2000).

61. Y. Zhou, X. Chen, C. Ko, Z. Yang, C. Mouli and S. Ramanathan, IEEE Electron Device Letters **34** (2), 220-222 (2013).

62. G. Seo, B.-J. Kim, C. Ko, Y. Cui, Y. W. Lee, J.-H. Shin, S. Ramanathan and H.-T. Kim, Electron Device Letters, IEEE **32** (11), 1582-1584 (2011).

63. B.-G. Chae, H.-T. Kim, D.-H. Youn and K.-Y. Kang, Physica B: Condensed Matter **369** (1), 76-80 (2005).

64. Y. Zhao, J. Hao, C. Chen and Z. Fan, Journal of Physics: Condensed Matter **24** (3), 035601 (2011).

65. Z. Yang, S. Hart, C. Ko, A. Yacoby and S. Ramanathan, Journal of Applied Physics **110** (3), 033725 (2011).

66. L. A. Gea and L. Boatner, Applied physics letters **68** (22), 3081-3083 (1996).

67. M. A. Kats, D. Sharma, J. Lin, P. Genevet, R. Blanchard, Z. Yang, M. M. Qazilbash, D. Basov, S. Ramanathan and F. Capasso, Applied Physics Letters **101** (22), 221101 (2012).

68. G. Seo, B.-J. Kim, H.-T. Kim and Y. W. Lee, Current Applied Physics **14** (9), 1251-1256 (2014).

69. Y. Vlasov and S. McNab, Optics express **12** (8), 1622-1631 (2004).

70. O. P. Parida and N. Bhat, presented at the Proceedings of the International Conference on Optics and Photonics, Chandigarh, India, 2009 (unpublished).

71. M. A. Meitl, Z.-T. Zhu, V. Kumar, K. J. Lee, X. Feng, Y. Y. Huang, I. Adesida, R. G. Nuzzo and J. A. Rogers, Nature Materials **5** (1), 33-38 (2005).

72. K. Zhang, J.-H. Seo, W. Zhou and Z. Ma, Journal of Physics D: Applied Physics **45** (14), 143001 (2012).

73. C. Ko and S. Ramanathan, Applied Physics Letters **93** (25), 2101 (2008).

74. H. Buhay, K. Kogler, B. Whitehead and R. Tiberio, Journal of Vacuum Science & Technology A **4** (3), 440-442 (1986).

75. J. C. Fan, H. R. Fetterman, F. J. Bachner, P. M. Zavracky and C. D. Parker, Applied physics letters **31** (1), 11-13 (1977).

76. Y.-H. Ham, A. Efremov, N.-K. Min, H. W. Lee, S. J. Yun and K.-H. Kwon, Japanese Journal of Applied Physics **48** (8S1), 08HD04 (2009).

77. T. Lee, A. Efremov, Y.-H. Ham, S. J. Yun, N.-K. Min, M. Hong and K.-H. Kwon, Journal of Micro/Nanolithography, MEMS, and MOEMS **8** (2), 021110-021110-021115 (2009).

78. H. Guckel, S. Larsen, M. Lagally, G. Moore, J. Miller and J. Wiley, Applied Physics Letters **31** (9), 618-619 (1977).

79. M. Konagai, M. Sugimoto and K. Takahashi, Journal of crystal growth **45**, 277-280 (1978).

80. R. C. Jaeger, Introduction to Microelectronic Fabrication **2**, 43-54 (2001).

81. H. Lorenz, M. Despont, N. Fahrni, N. LaBianca, P. Renaud and P. Vettiger, Journal of Micromechanics and Microengineering **7** (3), 121 (1997).

82. J. K. Steach, J. E. Clark and S. V. Olesik, Journal of applied polymer science **118** (1), 405-412 (2010).

83. K. K. Lee, D. R. Lim, H.-C. Luan, A. Agarwal, J. Foresi and L. C. Kimerling, Applied Physics Letters **77** (11), 1617-1619 (2000).

84. Y. Osano and K. Ono, Journal of Vacuum Science & Technology B **26** (4), 1425-1439 (2008).